LANGMUIR

pubs.acs.org/Langmuir Article

Computational Design of Nanostructured Soft Interfaces: Focus on Shape Changes and Spreading of Cubic Nanogels

Chandan Kumar Choudhury, Vaibhav Palkar, and Olga Kuksenok*



Cite This: https://dx.doi.org/10.1021/acs.langmuir.9b03486



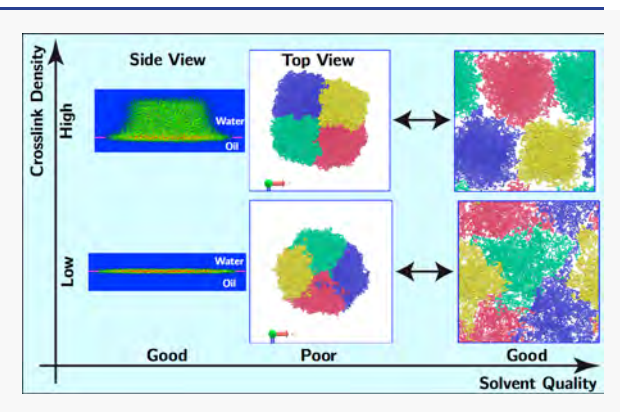
ACCESS

III Metrics & More

Article Recommendations

Supporting Information

ABSTRACT: Understanding the dynamics of gels at soft interfaces is vital for a range of applications, from biocatalysis and drug delivery to enhanced oil recovery applications. Herein, we use dissipative particle dynamics simulations to focus on the shape changes of a cubic nanogel as it adsorbs from the aqueous phase onto the oil—water interface, effectively acting as a compatibilizer. Upon adsorption at the interface, the hydrogel spreads over the interface, adopting various shapes depending on its size and cross-link density. We characterize these shapes by the shape anisotropy and an effective extent of spreading. We highlight the differences between these characteristics for cubic and spherical nanogels and show that the choice of the cubic shape over the spherical one results in a wider range of topographies that could be dynamically prescribed onto the soft interface due to the gels' adsorption. We first validate our model parameters with respect to the



known experimental values for polyacrylamide (PAAm) gels and focus on spreading and shape changes of PAAm nanogels onto the oil—water interfaces. We then probe the behavior of active gels by changing an affinity of the polymer matrix for the solvent, which can be caused by the application of an external stimulus (light, temperature, or change in the chemical composition of solvent). Furthermore, we focus on the interactions between multiple gels placed at the liquid—liquid interface. We show that controlling the shapes and the clustering of the gels at the interfaces via variations in solvent quality result in tailoring the dynamics and topography of soft nanostructured interfaces. Hence, our findings provide insights into the design of soft active nanostructured interfaces with topographies controlled externally via solvent quality.

■ INTRODUCTION

Shape changes often play a critical role in nature to ensure specific functional responses; examples range from leaves opening for sun tracking in plants and the projectile dispersion of seeds1 to shape changes observed in biological cells upon their adhesion to various surfaces.² Natural materials inspire the design of various synthetic shape-morphing materials with a range of dynamically actuated properties. A number of shape-morphing systems are hydrogel-based since hydrogels can be readily functionalized to respond to multiple stimuli such as changes in pH, temperature, and solvent quality.³⁻⁶ In addition, hydrogels can be filled with magnetic nanoparticles, whereby the shape and functionality of hydrogels can be controlled by the external magnetic field. The major drawbacks of using hydrogels as shape-morphing materials are their relatively low mechanical strength and slow response limited by the collective diffusion coefficient of the polymer matrix. The mechanical strength can be improved by utilizing strong dual cross-linked hydrogels,9 and the response time can be reduced by significantly decreasing the size of the samples. Recent advances allow one to accurately tailor the size of the gels and to fabricate functional nanogels with sizes within the range of 20-500 nm¹⁰ or even ultrafine nanogels with sizes

below 20 nm. ¹¹ Furthermore, the shapes of stimuli-responsive hydrogels can be readily tailored within a wide range. ^{1,12,13} Variations in shape, size, and rigidity can be utilized to optimize the biological response and the in vivo performance of nanoengineered delivery vectors. ^{14–16} In particular, cubic polymeric microparticles showed an enhanced uptake by breast cancer cells because they have a larger contact area with the cell compared to the spherical particles. ^{16,17}

Herein, we focus on the dynamics of shape changes of hydrogel particles upon their adsorption onto liquid—liquid interfaces. We show that the adsorption dynamics, equilibrium shape, and extent of spreading of cubic gels depend on the polymer matrix affinity for phases, gel sizes, and cross-link densities. Hence, using nanogels with different shapes and cross-link densities and tailoring their affinity to the solvent via external stimuli can offer a route to tailoring the topography of soft nanostructured active interfaces. A number of prior studies

Special Issue: Advances in Active Materials

Received: November 7, 2019 Revised: January 12, 2020 Published: January 13, 2020



focused on the adsorption of hydrogels at air–liquid 3,18,19 and liquid–liquid $^{3,20-22}$ interfaces. Widespread interest in the behavior of hydrogels at interfaces is largely due to various potential applications of these systems, including stimuli-tunable microlenses, soft emulsifiers, 24,25 biocatalysts, 24,26 and drug delivery. For example, the encapsulation of a single enzyme within a nanogel can enhance the biocatalytic activity of the enzyme and improve its stability. 26,27 With respect to gels adopting various shapes at the interfaces, spherical hydrogel particles adsorbed at liquid-liquid interfaces were shown to flatten at the oil-water interface, with the flattening most pronounced for hydrogels with low cross-link densities and small dimensions. Note that the distinct core–shell structure of the microgels in solution results in a "fried-egglike" shape at the interface, where the corona of the gel is flattened significantly more than the core with a higher crosslink density.²⁵ In addition, the hydrogels interacting with the same strength with both liquids were shown to extend symmetrically into both phases, resulting in the formation of the homogeneous mixture between the two phases within the gel.^{20,28} Note that polymer-grafted nanoparticles were also shown to localize and self-assemble at oil-water interfaces. 30,31

A variety of active microgels based on either polyacrylamide (PAAm) or poly-N-isopropylacrylamide (PNIPAAm) polymer matrixes have been fabricated by incorporating light-sensitive moieties such as azobenzene,^{32,33} triphenylmethane leuco,³⁴ spyropyran derivatives,³⁵ and redox-active units.^{36–38} Furthermore, light-induced reversible switching of the degree of swelling of microgel particles can be triggered by photoisomerization and the binding/unbinding of an azobenzenecontaining surfactant. In this case, a stepwise application of UV and blue light results in effective variations in the hydrodynamic radius of the microgels between ~580 and ~340 nm.³² The temperature-induced volume phase transition of PNIPAAm-based or poly(N-vinylcaprolactam) (PVCL)-based microgels can be used to control their spreading at interfaces. 18,39,40 Note that both PNIPAAm and PVCL have a lower critical solution temperature (LCST) of around 32 °C.41 Recently synthesized amphiphilic PVCL-based microgels exhibited a shift in the volume phase transition temperature to lower values with an increase in the hydrophobic content, and the corresponding spreading of these microgels at the solid surface was also regulated by the hydrophobic content.⁴⁰ Furthermore, the variation in temperature was shown to control the dynamic interfacial tension in microgel solutions adsorbing onto the toluene interface. Herein, a range of copolymer microgels based on VCL, NIPAAm, and Nisopropylmethacrylamide (NIPMAm) with various copolymer compositions were considered.³⁹ Such responsive microgels can be utilized in multiple applications, including the design of soft responsive emulsion stabilizers.⁴² In the above examples, the affinity between the polymer and solvent changes dynamically with an application of the external stimulus. In what follows, we will mimic the effects of application of external stimuli by changing the affinity of the polymer matrix for the solvent.

Despite significant progress in understanding the behavior of micro- and nanogels at interfaces, among the open questions remaining to be addressed are the effects of the shape of the gel particle on its interaction with the liquid—liquid interface and dynamic shape changes of active nanogels and their arrays adsorbed onto the interface in response to the changes in various external stimuli (temperature, light, and solvent

quality). Taking into account that a number of synthesis routes recently became available for fabricating hydrogels of various shapes, 3,13,16,17,43 an understanding of the effect of the gel shape on its spreading over the interface and the overall topography of the soft nanostructured interface would ultimately allow one to address potential advantages and limitations of a given choice of a shape of the gel particle. Below, we primarily focus on cubic samples and compare the dynamics of spreading for cubic and spherical gels. Specifically, we first focus on PAAm hydrogels; PAAm gels find their uses in numerous applications involving liquid-liquid interfaces, from enhanced oil recovery applications 44 to a variety of drug delivery applications encompassing contrast imaging,⁴⁵ targeted cancer chemotherapy,⁴⁶ and bioadheasive nanogel design. 47 We first validate our model parameters with respect to the known experimental values for PAAm gels and focus on spreading and shape changes of PAAm nanogels onto interfaces. We then probe the behavior of active nanogels by changing the affinity of the polymer matrix for the solvent. These changes effectively mimic changes in the degree of swelling of polymer matrixes under various stimuli such as light and temperature and in response to the change in the chemical composition of the solvent. In what follows, we characterize the dynamics and extent of spreading at the interfaces as a function of gel properties (cross-link density and size of the network) and probe the structural transitions in gels and nanostructured interfaces containing multiple gels in response to the change in solvent quality.

MODEL

We use the dissipative particle dynamics (DPD) approach 48,49 to simulate the dynamics of polymer gels. A known advantage of DPD is that it reproduces correct hydrodynamic behavior, 50 hence it has been used in simulations of a variety of complex mesoscale systems. The particles (or beads) in DPD represent collections of atoms; the motion of these particles is governed by Newton's equations of motion 49

$$\frac{\mathrm{d}\mathbf{r}_{i}}{\mathrm{d}t} = \mathbf{v}_{i}, \ \frac{\mathrm{d}\mathbf{p}_{i}}{\mathrm{d}t} = \sum_{j \neq i} \mathbf{F}_{ij} \tag{1}$$

where \mathbf{r}_{ij} \mathbf{v}_{ij} and $\mathbf{p}_i = m_i \mathbf{v}_i$ are the position, velocity, and momentum vectors of a particle i, respectively, and \mathbf{F}_{ij} is the pairwise additive force exerted on a particle i by a particle j with the summation over all of the particles within the chosen cutoff radius r_c . This cutoff radius introduces a characteristic length scale into the system⁴⁹ so that $r_c = 1$ in dimensionless DPD units. The masses of the particles are identical, $m_i = m$. The total force in eq 1 consists of three contributions: $\mathbf{F}_{ij} = \mathbf{F}_{ij}^{\mathrm{C}} + \mathbf{F}_{ij}^{\mathrm{D}} + \mathbf{F}_{ij}^{\mathrm{R}}$, where $\mathbf{F}_{ij}^{\mathrm{C}}$ is a purely repulsive conservative force, $\mathbf{F}_{ij}^{\mathrm{D}}$ is a dissipative force, and $\mathbf{F}_{ij}^{\mathrm{R}}$ is a random (stochastic) force. We chose the conservative force based on the soft repulsion potential

$$\mathbf{F}_{ij}^{C} = \begin{cases} a_{ij} \left(1 - \frac{r_{ij}}{r_{c}} \right) \mathbf{e}_{ij} & (r_{ij} < r_{c}) \\ 0 & (r_{ij} \ge r_{c}) \end{cases}$$

$$(2)$$

where a_{ij} is the maximum repulsion between particles i and j and $r_{ij} = |\mathbf{r}_{ij}|$ is the distance between the centers of mass of particles i and j, with $\mathbf{r}_{ij} = \mathbf{r}_i - \mathbf{r}_j$ and $\mathbf{e}_{ij} = \frac{\mathbf{r}_{ij}}{r_{ij}}$. We note that

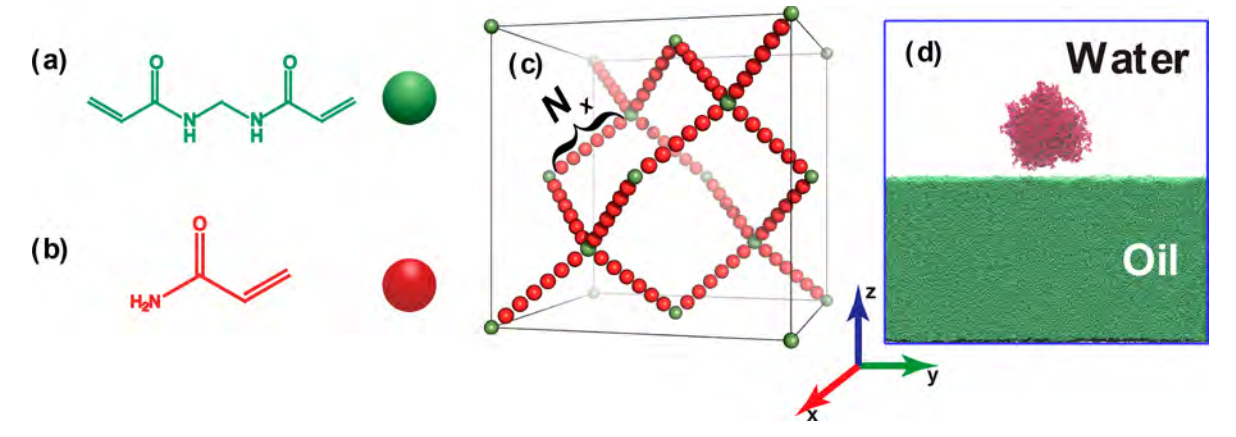


Figure 1. Chemical structures of (a) the N,N'-methylenebis(acrylamide) (MBAM) cross-linker, represented as a green bead, and (b) the acrylamide monomer, represented as a red bead. (c) $1 \times 1 \times 1$ hydrogel unit cell. (d) Initial setup (after equilibration): $3 \times 3 \times 3$ unit cell with $N_x = 30$ in the water phase, placed next to the oil phase (in green). Here and in all of the snapshots below, water beads are hidden for clarity.

while the soft repulsion potential is the most common choice in DPD allowing for the large integration steps, other choices of conservative potentials are possible ⁵¹ depending on the systems of interest. Two remaining contributions to the total force are written as ⁵²

$$\mathbf{F}_{ij}^{\mathrm{D}} = -\gamma \omega^{\mathrm{D}}(r_{ij})(\mathbf{e}_{ij} \cdot \mathbf{v}_{ij})\mathbf{e}_{ij}$$
(3)

$$\mathbf{F}_{ij}^{R} = \sigma \omega^{R}(r_{ij}) \zeta_{ij} \Delta t^{-1/2} \mathbf{e}_{ij}$$
(4)

where γ and σ are the strengths of the dissipative and random forces and $\mathbf{v}_{ij} = \mathbf{v}_i - \mathbf{v}_j$ is the relative particle velocity. Both dissipative and random forces also act along \mathbf{e}_{ij} . The ζ_{ij} in eq 4 is a symmetric Gaussian random variable with zero mean and unit variance:

$$\left\langle \zeta_{ij}(t) \right\rangle = 0, \left\langle \zeta_{ij}(t) \zeta_{ij}(t') \right\rangle = (\delta_{ik}\delta_{jl} + \delta_{il}\delta_{jk})\delta(t - t')$$
(5)

The condition $\zeta_{ij} = \zeta_{ji}$ is required for the conservation of total momentum.⁵³ The factor $\Delta t^{-1/2}$ in eq 4 ensures that the mean diffusion over any physical time interval has a finite value independent of the integration step Δt .⁴⁹

The dissipative and random forces (eqs 3 and 4) are coupled through the fluctuation—dissipation theorem. ⁵³ To ensure that the correct thermodynamic equilibrium state is reached, the following two conditions are imposed: ⁴⁹

$$\omega^{D}(r_{ij}) = [\omega^{R}(r_{ij})]^{2}, \, \sigma^{2} = 2\gamma k_{B}T/m$$
 (6)

 $k_{\rm B}$ is the Boltzmann constant, and T is the equilibrium temperature. The first condition in eq 6 couples the weight functions, and the second one couples the strengths of the random and dissipative forces and sets the temperature in the system. We chose the weight functions to have the same form as the conservative force 49

$$\omega^{R}(r_{ij}) = \begin{cases} \left(1 - \frac{r_{ij}}{r_{c}}\right) & (r_{ij} < r_{c}) \\ 0 & (r_{ij} \ge r_{c}) \end{cases}$$

$$(7)$$

Notably, while the soft potential choice for the weight function in eq 7 is the common choice in DPD, other choices are also permitted⁵¹ as long as the conditions in eq 6 are satisfied. For

the bonded interactions, we consider beads to be connected by harmonic bonds with the interaction potential

$$U_{\text{bond}} = K_{\text{bond}} (r_{ij} - r_{\text{b}})^2 \tag{8}$$

where K_{bond} is an elastic (spring) constant and r_{b} is an equilibrium bond distance. To integrate the above equations of motion (eq 1), we use a modified velocity Verlet algorithm. 45 In effect, DPD can be thought of as a thermostat which accurately reproduces hydrodynamic interactions.⁵⁰ In our studies, we use the DPD module as implemented in the LAMMPS simulation package. 54,55 Below, we introduce the DPD formulation for the gel matrix with tetrafunctional junctions and relate the DPD parameters chosen herein to the known experimental values for PAAm gels as well as to the continuum framework. We then use this validated model to focus on the interactions of the cubic PAAm gels with the oilwater interface. Finally, we note that along with well-known advantages of DPD, one of the limitations of this approach is an unphysical crossing of polymer chains, which is essentially a payoff for using a soft repulsion potential. To estimate an effect of bonds crossing on the hydrogel shape changes used in this study, we implemented the modified segmental repulsion potential (mSRP)⁵⁶ DPD approach and showed that the characteristics of spreading remain essentially unaffected (see below).

Introducing the Polymer Network. We first introduce a framework for a PAAm gel interacting with the oil-water interface. The polymerization of an aqueous solution of acrylamide in the presence of a small amount of tetrafunctional cross-linker, methylenebis(acrylamide) (MBAM), results in the formation of a macroscopic 3D network of PAAm provided that the ratio between the concentration of a cross-linker and monomers exceeds a critical value.⁵⁷ The two double bonds in MBAM (Figure 1a) result in the formation of four covalent bonds with neighboring molecules. The polymer gel matrix consists of acrylamide strands interconnecting at the MBAM tetrafunctional junctions. Both an acrylamide monomer and a MBAM cross-linker are represented by a single bead each (Figure 1a,b). The initial configuration of the "unit cell" of a PAAm gel matrix is modeled as a diamondlike lattice 58-60 (Figure 1c), where the lattice points are occupied by the tetrafunctional cross-links and the basis positions are connected by the acrylamide monomer strands. The number of acrylamide beads between the cross-linkers is denoted by N_x (Figure 1c, red beads). The dangling ends at the basis positions on the surface of the diamond lattice with a connectivity of less than 4 were retained without any modifications.⁶⁰ This diamondlike lattice (Figure 1c) was replicated in the x, y, and z directions to form gel samples of various sizes. We use the convention $I \times J \times K$ to refer to the nanogel size, where I, I, and K denote a number of replicas in the x, y, and z directions, respectively. Each lattice was prepared with a polymer strand length of $N_x = 15$, 20, 25, or 30. To investigate the effect of the cross-link density, we prepared $2 \times 2 \times 2$, $3 \times 3 \times 3$, and $4 \times 4 \times 4$ gels with $N_x =$ 48, 14, and 6, respectively; these three systems have similar numbers of polymer beads. The details of our simulated gel networks are listed in Table S1. The gel networks were preequilibrated in the water phase only and then placed in the water phase in the oil-water system (Figure 1d). Gel and water beads together constituted 50% of the volume in these simulations, while the other 50% was occupied by oil. Each simulation run below was repeated four times with different initial coordinates, initial random velocities, and random forces. We also prepared systems with four gels as detailed below. Periodic boundary conditions were applied in all three directions in all of the simulations.

Simulation Parameters and Relationship between These Parameters and Experimental Values. The repulsion parameter between the water beads and between the same type of beads is taken as $a_{ii} = 78 \frac{k_B T}{r_c}$, which is calculated on the basis of the compressibility of water at room temperature for the degree of coarse-graining set as N_m = 3.48,49 The same degree of coarse-graining and the same repulsion parameter had been used in DPD simulations of various systems, from Nafion membranes⁶¹ to PAAm chains⁶² or asphaltene-PAAm chains⁶³ in oil-water emulsions. Thereby, three water molecules are represented by a single bead, 48 while four oil beads form an oil molecule with each bead representing three CH₂ groups. 48,62 The repulsion coefficient for the dissimilar beads can be estimated on the basis of the affinity between those beads as $a_{ij} = a_{ii} + 3.27 \chi_{ij}$, where χ_{ij} is the Flory–Huggins polymer–solvent interaction parameter. For PAAm gels in water, $\chi_{\rm PW} = 0.48$ gives $\chi_{\rm PW} = 79.57$. (Herein and in the following description, the values of $\chi_{\rm PW} = 0.48$) are provided in reduced DPD units, $\frac{49}{r_c} \frac{k_B T}{r_c}$). We note that to accurately reproduce the swelling of gels one needs to account for the dependence of the Flory-Huggins interaction parameter χ_{PW} on the polymer volume fraction (for details, see the section on the comparison with continuum theory below), which in turn results in an increase in a_{PW} . Hence, we set $a_{PW} = 80$ for the polymer-water interaction and a significantly higher value for the water—oil repulsion as a_{WO} = 100.⁶² In addition, we simulated a linear PAAm chain with a length of N beads in water and a polymer chain representing an oil in water with $a_{PW} = 80$ and 100, respectively. The

Finally, to simulate the shape changes of active stimuliresponsive gels in response to changes in external stimuli, we varied the solvent quality from good to poor by varying the gel—solvent repulsion parameter a_{PS} . A list of all of the system

dependence of the mean square radius of gyration $\langle R_{\rm g}^2 \rangle$ on the chain length $\langle R_{\rm g}^2 \rangle \propto (N-1)^{2\nu}$ gives anticipated values for the scaling exponent, 66 ν , with $\nu=0.558$ and 0.304 for PAAm in

water (good solvent) and oil in water (poor solvent),

respectively.62

parameters is given in Table S2. These changes effectively mimic the change in the affinity of the polymer matrix for the solvent under various stimuli such as light and temperature and in response to the change in the chemical composition of the solvent. In what follows, we characterize the dynamics and extent of spreading at the interfaces as a function of gel properties (cross-link density and the size of the network) and probe the structural transitions in gels and nanostructured interfaces containing multiple gels with a response to the change in solvent quality.

The total number density in the box was kept at $3r_c^{-3}$, and

the bond constant and the equilibrium bond length were set to

 $500\frac{k_{\rm B}T}{2}$ and $0.7r_{\rm cl}$ respectively.²² The cutoff radius $r_{\rm cl}$ temperature, and mass of a bead are set equal to 1.0 in reduced DPD units.^{48,49} The strength of the random force is chosen as $\sigma = 3$, and the time step is set at 0.02τ ; the unit of energy is k_BT . The system sizes (box dimensions and number of beads) are listed in Table S3. The simulations are performed for 3×10^6 steps. The above choice of the degree of coarsegraining with three water molecules representing a single bead allows one to relate the dimensionless value of r_c to the corresponding dimensional value of 0.646 nm. 49 The dimensionless unit of time can be related to the characteristic dimensional value τ by relating the diffusion coefficient of water beads D_{sim} to a known value of the dimensional diffusion coefficient of water $D_{\rm water}$ as 48,49 $au=\frac{N_{\rm m}D_{\rm sim}r_{\rm c}^2}{D_{\rm water}}$. We calculate the dimensionless diffusion coefficient of water beads D_{sim} by averaging a mean square displacement over five runs of 5×10^4 time steps each and determining the slope of $r_{\rm w}^{2}(t)/6$ against time and find $D_{\text{sim}} = 0.1487(12)$. Using $D_{\text{water}} = 2.43 \times 10^{-5}$ c m^2/s , we obtain $\tau = 76.6$ ps. With this scaling, the linear size of the cubic samples in the water phase ranges from approximately 14 to 37 nm, exhibiting a significant extension along the interface during the spreading. In what follows, we will provide the values of time and size in reduced DPD units estimated above. It is worth noting that the dimensionless units in DPD can also be related to macroscopic parameters depending on the problem of interest and a set of macroscopic properties that needs to be reproduced in the given problem. 67 In the latter cases, the DPD reduced units can significantly exceed the above estimates; however, other properties such as the dimensionless compressibility of solvent discussed above are no longer reproduced.⁶⁷ We also note that DPD simulations of spherical gels with sizes similar to the sizes of cubic samples used herein (in reduced DPD units) have been performed, 20,28,68 and these simulation showed a good correspondence with the behavior of microgels at oil-water interfaces observed in concurrent experiments.⁶⁹

■ RESULTS AND DISCUSSION

Comparison with Continuum Theory. We first relate our DPD approach to the continuum theory of polymer networks and compare characteristic values obtained from our simulations with the existing experimental data on PAAm networks. Hence here we first analyze the equilibrium swelling of a number of gel samples placed only in a water phase (Table S3). Hydrogels in a solvent undergo swelling depending on the quality of solvent and the elasticity of the polymer network. We calculate an equilibrium polymer volume fraction, ϕ , by calculating the fraction of polymer beads within a sphere with the radius set by the radius of gyration as $R_{\rm g}/\sqrt{3}$. The center

of the sphere is chosen at the center of mass of the gel particle. In such a manner, we focus only on the properties of the core of the gel particle.

At a continuum level, the swelling is often described by the Flory–Rehner (FR) theory, which takes into account osmotic and elastic pressures acting on the hydrogel network. The balance of osmotic and elastic stresses in equilibrium is given by the FR equation⁷⁰

$$\phi + \chi(\phi)\phi^{2} + \ln(1 - \phi) - c_{0} \left(\frac{\phi}{2\phi_{0}} - \left(\frac{\phi}{\phi_{0}}\right)^{1/3}\right) = 0$$
(9)

where c_0 is the dimensionless parameter proportional to the number density of junction points (cross-links) as defined below, $\chi(\phi)$ is the interaction parameter capturing the affinity between the polymer and solvent, and ϕ_0 is the volume fraction of polymer in the reference state (during preparation). Parameter c_0 in eq 9 is defined via the number density of elastically active polymer strands calculated in reference state ν as $c_0 = \frac{\nu V_{\rm s}}{N_{\rm A}}$ (note that for the tetrafunctional network, the number of junction points is a half of the number of elastically active strands⁷⁰), N_A is Avogadro's number, and V_s is the molar volume of solvent $(18 \times 10^{-6} \text{ m}^3 \text{ mol}^{-1})$. The above framework corresponds to affine deformations of a polymer network. An affine network model is the simplest network model that captures rubber elasticity and is able to account for the network deformability based on the entropic elasticity of polymer chains. For the phantom network model, c_0 in eq 9 needs to be replaced by $c_0^{\rm ph} = \left(1 - \frac{2}{f}\right)c_0$, where f is the functionality of the network (f = 4 for the tetrafunctional)PAAm network). c_0 can be estimated as⁷¹ $c_0 = \frac{V_{\rho_p} \phi_0}{N_{\nu} M_0}$, where ρ_p is the mass density of polyacrylamide polymer⁷² $(1.35 \times 10^{-6} \text{ g})$ m^{-3}), M_0 is the molar mass of a monomer (71 g mol⁻¹), and N_x is the number of monomers within one polymer strand. In experiments, ϕ_0 can be varied by changing the concentration of polymer during synthesis. ^{64,65,73} Notably, an affine assumption could break down for sufficiently low⁷⁴ ϕ_0 . We use an experimentally relevant value of $\phi_0 = 0.15^{64,65}$ in our analysis to first calculate c_0 as given above and then solve eq 9 for ϕ and fit this solution with the values calculated from DPD simulations (black solid line in Figure 2). The error bars indicate the standard deviation for more than 500 samples taken from 1 simulation run at different instants in time after the system reached equilibrium.

We take the polymer–solvent interaction parameter in eq 9 to be $\chi(\phi) = \chi_0 + \chi_1 \phi + \chi_2 \phi^2$. The same functional dependence for $\chi(\phi)$ has been used to fit experimental data for PAAm gels⁶⁴ (herein only the linear term was used with $\chi_2 = 0$), in a theoretical study of PAAm gels,⁷⁵ in fitting experimental data on PNIPPAm gels,⁷¹ and in DPD simulations on PNIPPAm gels.^{76,77} On the basis of available experimental data, we set $\chi_0 = 0.48^{64,65}$ and find the best fit at $\chi_1 = 0.305$, $\chi_2 = 0.549$. Notably, a similar fitting can be obtained for a different value of ϕ_0 ($\phi_0 = 0.2$, $\chi_1 = 0.245$, $\chi_2 = 0.649$, fitting is not shown), which justifies the somewhat arbitrary choice of ϕ_0 . These fittings match well with the dependence predicted by Suekama et al.⁶⁴ Furthermore, this dependence also gives $\chi(\phi) \approx 0.49$ for $\phi \approx 0.01-0.1$, which is the value reported in experi-

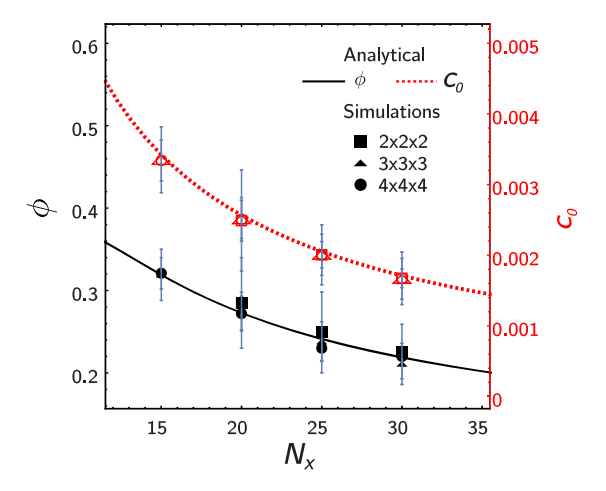


Figure 2. Polymer volume fraction ϕ (left y axis, solid line) and crosslink density c_0 (right y axis, dashed line) as functions of N_x . The solid and dashed lines are from respective analytical calculations. The symbols (filled for ϕ and unfilled for c_0) represent data points from simulations, where circles, triangles, and squares correspond to $4 \times 4 \times 4$, $3 \times 3 \times 3$, and $2 \times 2 \times 2$ gels, respectively.

ments. ^{64,65,78,79} This value of $\chi(\phi)$ in turn corresponds to repulsion parameter $a_{ii} = 80$ chosen in our DPD simulations.

In addition to analytical estimates of c_0 based on respective physical parameters, c_0 can also be calculated numerically from the DPD simulations using the relation $c_0^{\mathrm{DPD}} = \rho_\mathrm{c} \frac{\phi_0}{\phi} \frac{V_\mathrm{s}}{N_\mathrm{A}}$, where

 ρ_c is the number density of polymer strands in equilibrium. For each value of N_x , we calculate the number density of polymer strands in the swollen equilibrium state ρ_c within the same spherical volume as for ϕ . Nearly perfect matching between the analytically and numerically calculated values (c_0 and c_0^{DPD}) is evident in Figure 2 (dashed line and red symbols, respectively). Hence, our results show that an affine network approximation is a reasonable approximation describing the elasticity of the PAAm polymer network considered, which is consistent with prior DPD studies on PNIPAAm polymer gels. ^{76,80}

Finally, the shear modulus of a swollen hydrogel can be estimated for an affine network in a good solvent as 64,66

$$G = \tilde{G}c_0 \left(\frac{\phi}{\phi_0}\right)^{1/3}$$
, where $\tilde{G} = \frac{N_A k_B T}{V_s}$. At $T = 300$ K, $\tilde{G} \approx 138.5$

MPa, and the estimates for the gels considered in these simulations are in the range of 265–600 kPa owing to the high values of ϕ (similar high elastic moduli were observed experimentally for the gels with high polymer volume fractions⁸¹). Using the above functional dependence with the lower values of $\phi \approx 0.1$ brings G down to about 100 kPa, which corresponds to the experiments on the PAAm gels with similar polymer volume fractions.

Shape Changes and Dynamic Restructuring of a Cubic Nanogel at the Oil–Water Interface. To characterize the spreading dynamics and an equilibrium conformation of a hydrogel at the oil–water interface, in the series of independent simulations we varied the degree of polymerization of the strands between the junctions N_x , sample sizes, and cross-link densities. In our reference scenario, we first equilibrated a $3 \times 3 \times 3$ sample with $N_x = 30$ in water and placed the sample near the oil–water interface (Figure 1). The dynamics of this system effectively encompass two stages. During the first stage, the gel diffuses out of the water toward

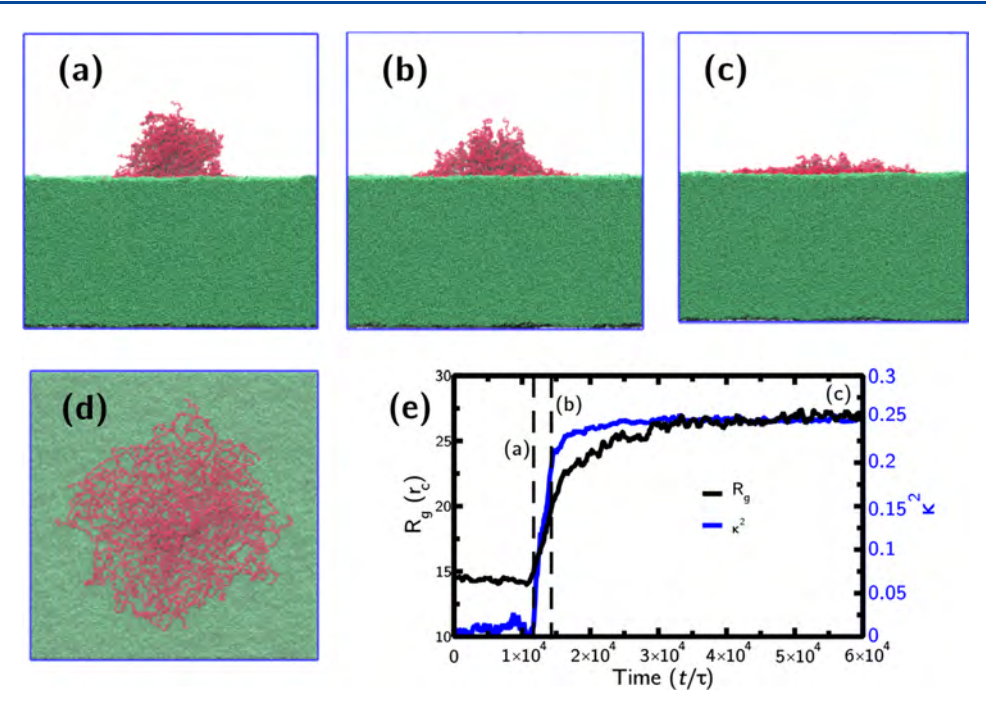


Figure 3. (a-d) Morphology snapshots for a $3 \times 3 \times 3$ $N_x = 30$ gel as it adsorbs onto the oil—water interface at (a) $1.17 \times 10^4 \tau$, (b) $1.43 \times 10^4 \tau$, and (c, d) $6 \times 10^4 \tau$ ((c) is a side view and (d) is a top view (xy plane)). (e) Time evolution of a radius of gyration (R_y , black curve, left axis) and shape anisotropy (κ^2 , blue curve, right axis). The time instances corresponding to the (a-c) snapshots are marked by the dashed lines in (e).

the interface until it contacts the interface, and during the second stage, it adsorbs onto the interface (Figure 3a-c). Adsorption onto the oil—water interface and spreading over this interface are energetically favorable because they minimize a number of unfavorable contacts between the immiscible water and oil beads. The equilibrium gel shape and the extent of gel spreading are defined by the interplay between the energy gain due to the shielding of the oil—water interface and the elastic energy payoff upon spreading. The side and top views (Figure 3c,d, respectively) of the nanogel at equilibrium show that the cubic gel considered herein flattens at the interface, which is consistent with prior studies showing the flattening of nanogels with spherical shapes. ^{21,25,28}

To quantify the shape and extent of spreading, we calculate the time evolution of the radius of gyration, $R_{\rm g}$, and the shape anisotropy, κ^2 . Both values are defined by the eigenvalues (λ_1 , λ_2 , λ_3) of the gyration tensor with the components $S_{xy} = \frac{1}{N^2} \sum_{i=1}^N \sum_{j>i}^N (x_i - x_j) (y_i - y_j)$. Here, the summation is taken over all beads within the nanogel. The squared radius of gyration, $R_{\rm g}^2$, is calculated as the first invariant of a diagonalized gyration tensor $S_{\rm p}$ as $R_{\rm g}^2 = I_1 = {\rm tr}([S_{\rm p}]) = \lambda_1 + \lambda_2 + \lambda_3$, and the shape anisotropy is defined as 82

$$\kappa^2 = 1 - 3\frac{I_2}{I_1^2} \tag{10}$$

where $I_2 = \lambda_1 \lambda_2 + \lambda_2 \lambda_3 + \lambda_3 \lambda_1$ and $\lambda_1 \ge \lambda_2 \ge \lambda_3$. Shape anisotropy is often used to characterize shapes of various objects with complex geometries including polymers with complex architectures. It is scaled between $\kappa^2 = 0$ for an object with high symmetry (for example, spherical or cubic symmetry) and $\kappa^2 = 1$ for the points located on a line. For a planar object with $\lambda_1 = \lambda_2$ and $\lambda_3 = 0$, $\kappa^2 = 0.25$. Finally, we define the extent of spreading at a given moment in time, $\alpha(t)$, as the ratio of the square root of the largest eigenvector (largest length estimate) of the gyration tensor at the interface, $\sqrt{\lambda_1}$, to

the same value calculated in water averaged over the last $2\times 10^4\tau$ in equilibrium $\langle\sqrt{\lambda_1^{\rm w}}\>\rangle.$ (Notably, all three eigenvalues in water are approximately the same.)

The time evolution of both κ^2 and R_g for the same simulation run is shown in Figure 3 (blue and black curves, respectively); herein, (a-c) marks correspond to the snapshots in Figure 3a-c. In the water phase, the nanogel retains its highly symmetric initial configuration (Figure 1d), hence $\kappa^2 \approx$ 0 until the time instant the gel comes into contact with the interface (Figure 3, blue curve). As the gel begins to spread over the interface, both κ^2 and R_{σ} increase, reaching their respective saturation values at equilibrium, with an apparent faster increase in the shape anisotropy κ^2 than in R_{σ} . Note that κ^2 plateaus at an equilibrium value of $\kappa^2 \approx 0.25$, confirming the close-to-planar morphology observed in Figure 3. Side views with the oil phase removed and an interface marked for the same time instances are shown in Figure S1a-c. We note that the adsorption of the cubic gels onto the interfaces and the subsequent flattening are consistent with the previously observed flattening of the spherical microgels at liquidliquid^{21,25,28} and air-liquid interfaces;¹⁹ we focus on the differences between the behavior of spherical and cubic microgels at interfaces further below.

Effect of Gel Size. Notably, such close-to-planar spreading is observed only for relatively small samples. To investigate an effect of the gel size on the shape anisotropy and the extent of spreading, we compared the dynamics and equilibrium characteristics of $2 \times 2 \times 2$, $3 \times 3 \times 3$, and $4 \times 4 \times 4$ gel matrices with $N_x = 30$. The equilibrated conformations for these gel sizes are shown in Figure S2a,b, Figure 3c,d, and Figure S2c,d, respectively. For the largest sample $(4 \times 4 \times 4)$, in addition to the spreading over the interface, a significant portion of the gel remains within the water phase. This is evident in Figure S2d and is confirmed quantitatively by calculating a shape anisotropy (Figure S2e) saturating at κ^2 =

 0.236 ± 0.003 (averaged over four independent runs). This value is lower than 0.25, indicating a deviation from the planar shape. The effect is more pronounced for gels with a larger size (Figure S2e) or lower N_x (Figure S2f).

Effect of N_x . In the next series of simulations, we focused on the 3 \times 3 \times 3 gel network with N_x = 15, 20, 25, 30. With an increase in N_x and a fixed number of cross links, the effective cross-link density decreases; however, the total number of polymer beads in these simulations also increases. (An effect of the cross-link density for gels with a matching number of polymer beads is considered in the section below.) As can be anticipated, the radius of gyration, Rg, also increases with an increase in N_x (Figure S3, red line). Notably, the ratio R_g/N_x saturates at approximately the same constant value, with the fastest saturation for the lowest N_x (Figure S4, black curve). An increase in N_x results in an overall slower spreading process, and for the highest value considered herein, saturation value R_{σ}/N_x is somewhat lower (blue curve in Figure S4). Furthermore, an increase in N_x also results in a lower elastic modulus (see the section above on the comparison with continuum theory) so that at higher N_r the penalty for gel deformation at the interface is lower and the sample is more readily able to adopt a close-to-planar conformation by maximizing the interfacial coverage. We find that the shape anisotropy, κ^2 , for $N_r = 30$ and 25 reaches values close to 0.25 at equilibrium, indicating a planar conformation, while a more densely cross-linked gel ($N_r = 15$) spreads considerably less (κ^2 \approx 0.2) (Figure S2f).

Effect of Cross-Link Density. To isolate the effects of crosslink density, we kept the number of gel beads close to the constant value for various N_x (choosing samples of $2 \times 2 \times 2$ for $N_x = 48$, $3 \times 3 \times 3$ for $N_x = 14$, and $4 \times 4 \times 4$ for $N_x = 6$ with the total number of gel beads 6144, 6048, and 6144, respectively). Hence, the $2 \times 2 \times 2$ sample has the lowest cross-link density and the smallest number of elastically active polymer strands, and the 4 × 4 × 4 sample has the highest cross-link density and the largest number of elastically active polymer strands. Correspondingly, the elastic energy penalty for spreading at the interface will be lowest for the $2 \times 2 \times 2$ sample and highest for the $4 \times 4 \times 4$ sample. (Recall that an affine network model that accounts for the network deformability based on the entropic elasticity of polymer chains is shown to be a good approximation for our polymer networks (see above).) The snapshots of the samples equilibrated at the interfaces (top view) for each of these gels are shown in Figure 4a,c,e. As the cross-link density increases, the gel morphology resembles its initial shape more strongly since the spreading is more restricted due to an increase in the elastic energy penalty. Figure 4b,d,f shows the 2D number density distribution of gels in the yz plane averaged over the x axis (perpendicular to the interface) for gels with N_x = 48, 14, and 6, respectively. These images show that an equilibrated gel morphology for a loosely cross-linked $(N_x =$ 48) gel (Figure 4a, top view) takes the shape of a thin layer spread over the interface (Figure 4b). Figure 4e,f shows the morphology snapshot and 2D-density distribution, respectively, for the densely cross-linked $(N_x = 6)$ gel. The spreading of this gel is restricted, and the gel takes a complex shape. The portion of the gel remaining in the water phase remains close to its initial cubic shape with a significant amount of water absorbed within the polymer matrix. The sample with an intermediate cross-link density ($N_x = 14$, Figure 4c,d), is highly deformed but does not form the thin layer observed for a

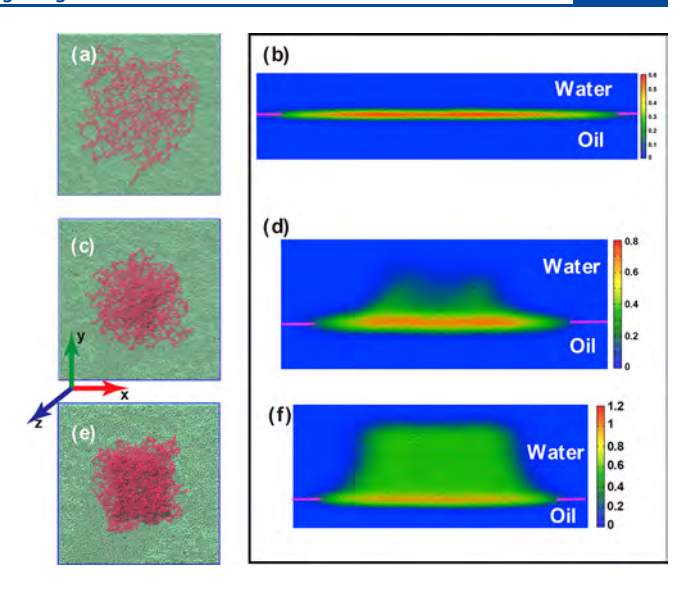


Figure 4. Equilibrated gel morphologies (top view, left column) and close-up polymer number density profiles in the yz plane averaged over the x axis (side view, right column) for matching numbers of polymer beads: (a, b) $2 \times 2 \times 2$, $N_x = 48$; (c, d) $3 \times 3 \times 3$, $N_x = 14$; and (e, f) $4 \times 4 \times 4$, $N_x = 6$. The cross-link density increases from top to bottom. The right column side-view images are the cut-out portions of the simulation box with the following y_1 , y_2 and z_1 , z_2 coordinates (in units of r_c) within the box: 12.5, 87.4 and 38, 58 for (b), 12.5, 32.5 and 17, 37 for (d), and 10, 30 and 18, 38 for (f).

loosely cross-linked gel. In this case, the gel is localized between the water and oil phases with the highest polymer volume fraction at the interface and somewhat protrudes into the oil phase. These observations demonstrate the effects of hydrogel elasticity on equilibrium shape. To estimate the effect of bond crossing on the observed shape changes and gel restructuring at the interface, we used the modified segmental repulsion potential (mSRP)⁵⁶ DPD approach and compared the evolution of the extent of spreading and the effective change in the thickness of the samples for the case of a densely cross-linked gel. Our results showed that these characteristics and the overall shape of the gel at the interface remain essentially unaffected (Figure SS).

The time evolution of both, the number of gel-oil contacts, n_{po} (Figure 5a), and the shape anisotropy, κ^2 (Figure 5b) from the moment the gel sample is in contact with the interface (this time instant differs for independent simulation runs) shows a gradual increase in these values during the spreading until the gels are equilibrated at the interface. We count a pair of beads to be in contact if the distance between them is within r_c . The number of gel-oil contacts is the highest for the loosely crosslinked $(N_x = 48)$ sample that undergoes the largest spreading (black curve in Figure 5; the equilibrium shape (side view) in this case is shown in Figure 4b). Correspondingly, the equilibrium values of the number of contacts are lower for the remaining two cases (red and green curves in Figure 5a). We note an increase in the size of error bars with an increase in N_x . An increase in N_x results in an increase in the fraction of dangling ends, hence some of the initial contacts are attributed entirely to dangling ends contacting only the interface or to the short contact with a small fraction of a polymer strand. Both the number of contacts and the shape anisotropy for all four independent runs for $N_x = 14$ and 48 are shown in Figure S6a,b,d,e, illustrating that the initial shape restructuring takes different times due to the increased effects of fluctuations for

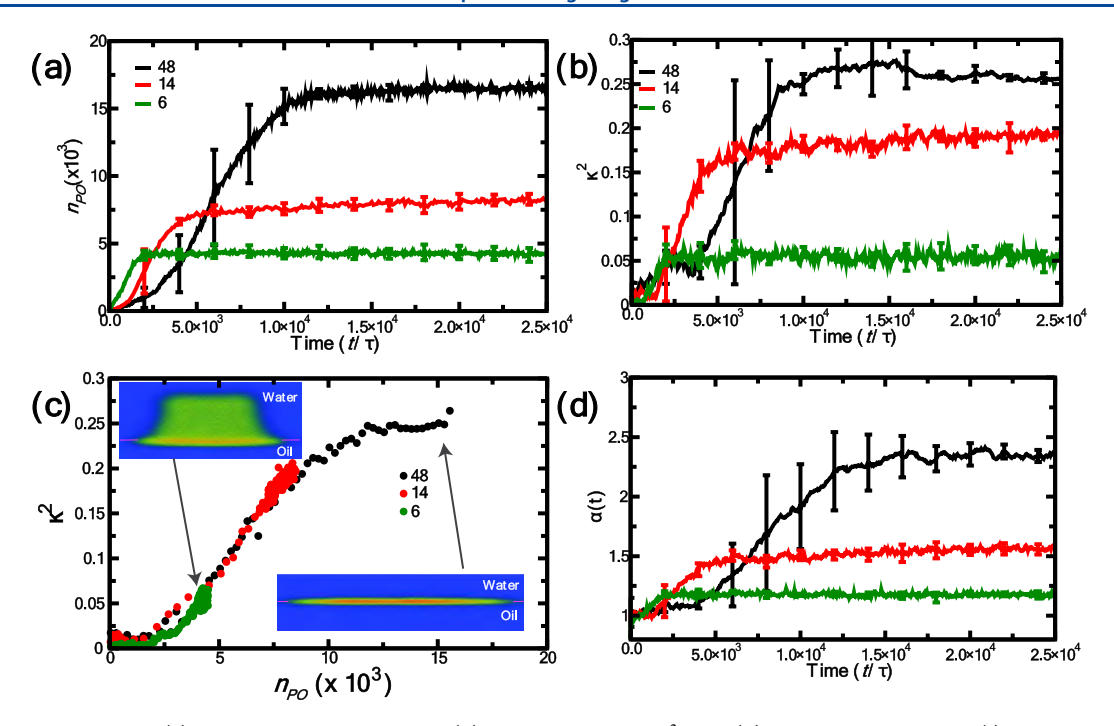


Figure 5. Time evolution of (a) polymer—oil contacts, n_{po} , (b) shape anisotropy, κ^2 , and (d) extent of spreading, $\alpha(t)$, for the simulation runs shown in Figure 4. All data points are averaged over four runs. $\langle \sqrt{\lambda_1^{\text{w}}} \rangle$ values for $2 \times 2 \times 2$, $N_x = 48$; $3 \times 3 \times 3$, $N_x = 14$; and $4 \times 4 \times 4$, $N_x = 6$ are 7.964, 5.837, and 5.039, respectively, in units of r_c . (c) Parametric plot of $\kappa^2(n_{\text{po}})$ using the data in (a) and (b). The black curve is superimposed onto the red and green curves. Time t = 0 in (a), (b), and (d) reflects the time the gel beads first come into contact with the oil beads.

larger N_x , leading to larger error bars while averaging over four independent runs. The densely cross-linked gel deforms to a smaller extent compared to the loosely cross-linked gels, which is reflected in the lower saturation values of κ^2 , and thus equilibrates faster. Interestingly, a parametric plot of the data in Figure 5a,b shows that all three cases follow the same curve, $\kappa^2(n_{po})$, with higher values reached for the loosely cross-linked gels (Figure 5c). Herein, the data averaged over runs for each of the cases is shown with the black curve superimposed onto the red and green curves, and the data for each individual run is provided in Figure S6c-f. The time evolution of the extent of spreading, $\alpha(t)$, also confirms that, owing to the lower elastic energy penalty, the spreading is more pronounced for the loosely cross-linked gel, which extends about 2.5 times with respect to its equilibrium size in water, and relatively small for the dense gel (Figure 5d). Notably, Figure 5a-d also shows that loosely cross-linked gels spread slower than densely crosslinked ones, and the same trends were observed in prior studies on the spreading of spherical gels with different cross-link densities.²¹ Thus, the network elasticity affects both the equilibrium and dynamic properties of hydrogels at interfaces.

Controlling the Extent of Spreading and Shape Anisotropy. To summarize how one can control the shape anisotropy and the equilibrium extent of spreading by varying the physical properties of the gel, we plot α (solid curves) and κ^2 (dashed curves) as a function of $1/N_x$ for all of the scenarios considered above (Figure 6). Recall that the dimensionless cross-link density defined in the continuum theory section (above), c_0 , is proportional to $1/N_x$. The extent of spreading decreases with an increase in cross-link density (decrease in N_x), with similar values of α for gels of different sizes (nearly overlapping red, green, and black solid curves). Notably, α is the highest for the loosely cross-linked gels and lowest for the densely cross-linked gels. These distinct cases (marked by blue

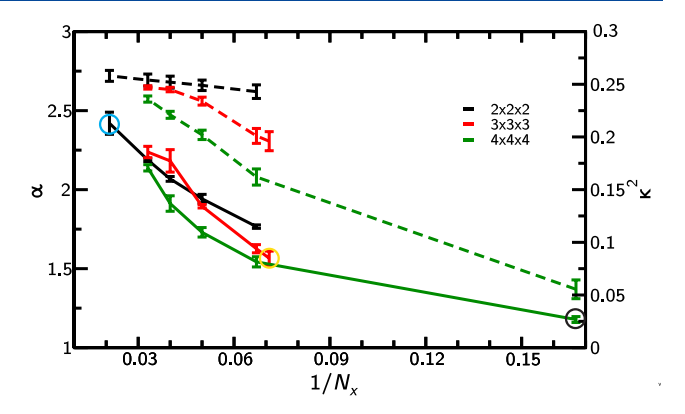


Figure 6. Equilibrium extent of spreading, α (left y axis, solid lines), and shape anisotropy, κ^2 (right axis, dashed line), as a function of $1/N_x$. The three open circles on the plot point to the gel with matching numbers of polymer beads (2 × 2 × 2, N_x = 48; 3 × 3 × 3, N_x = 14; and 4 × 4 × 4, N_x = 6; the simulation runs are in Figure 4).

and black circles) correspond to cases (b) and (f) in Figure 4. Summarizing the behavior of the shape anisotropy, κ^2 , we note that the close-to-planar spreading ($\kappa^2 \approx 0.25$) with the highest surface coverage is observed either for the small samples (black dashed curve) or in the limit of the low cross-link densities (observed trend at high N_x for the red and green curves). Finally, an average radius of gyration, $R_{\rm g}$, at the interface increases with N_x for all of the cases considered. This increase is the steepest for the $4 \times 4 \times 4$ samples and the lowest for the $2 \times 2 \times 2$ sample (Figure S3).

Comparison of the Spreading of Cubic and Spherical Gels. To elucidate the effect of shape, we compared the dynamics and an equilibrium extent of spreading for cubic and spherical nanogels with the matching number of polymer beads. For the case of the spherical gel, a sphere was inscribed

Langmuir pubs.acs.org/Langmuir Article

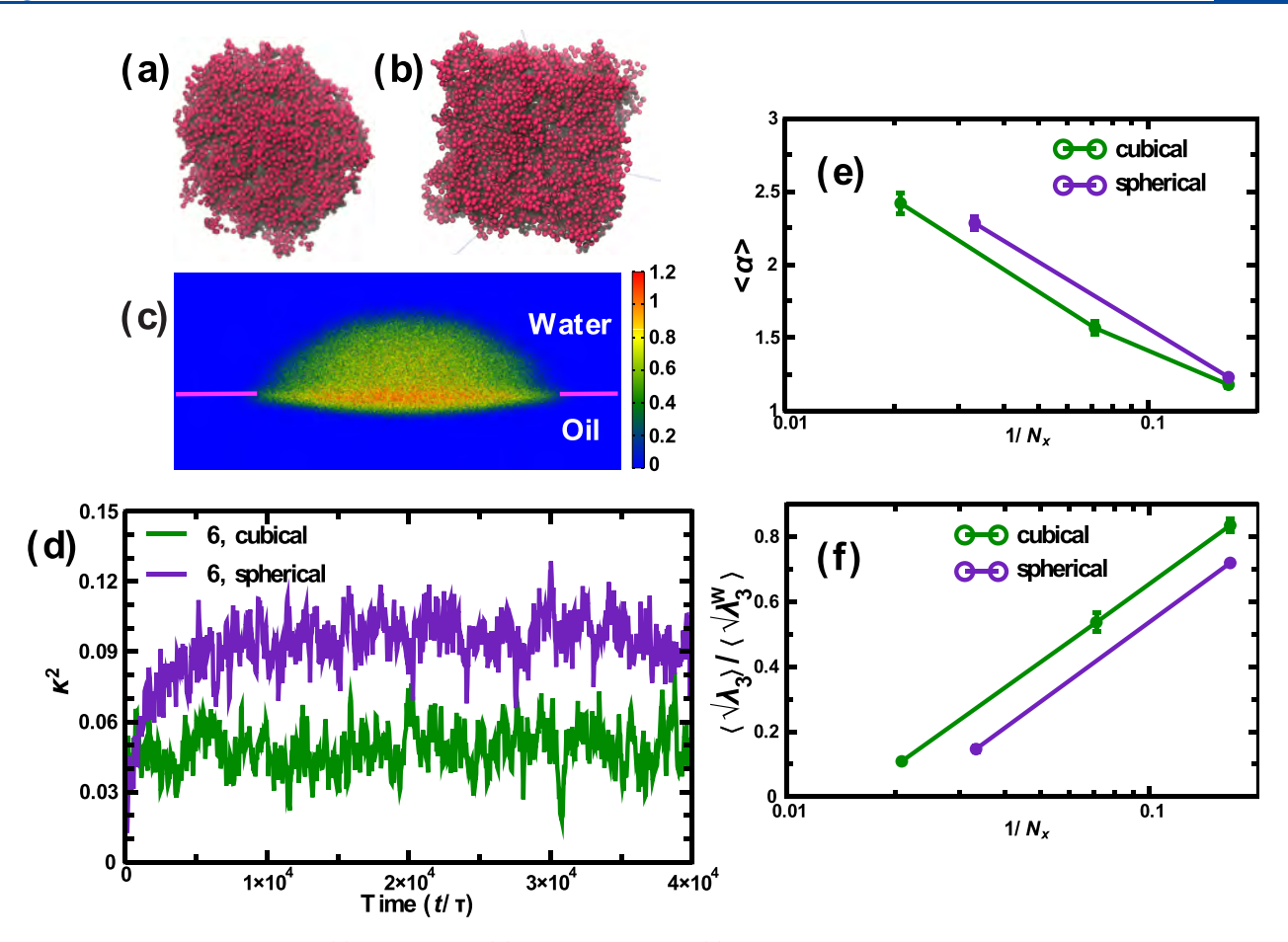


Figure 7. Equilibrated morphology of (a) spherical and (b) cubic gels in water. (c) Two-dimensional number density profile for the spherical gel at the interface. (d) Time evolution of κ^2 at the oil—water interface for cubic and spherical gels. (e) Extent of spreading, α , for spherical and cubic gels with a matching number of polymer beads. (f) Effective thickness of the gel in the direction perpendicular to the interface (normalized by the linear dimension in water) for cubic and spherical gels as a function of $1/N_x$.

1

within the $5 \times 5 \times 5$ gel with $N_x = 6$, and the beads outside the sphere were discarded. This spherical gel has a similar number of polymer beads to $4 \times 4 \times 4$, $N_x = 6$ cubic gels (Table S3). The swollen equilibrated morphology in water is shown in Figure 7 for spherical and cubic gels. These gels retain their geometrical shape in water due to the relatively high cross-link density. Upon adsorption at the oil-water interface, the spherical gel adopts a hemispherical shape (Figure 7c), which is consistent with the number of prior studies on spherical gels. 25,29 Notably, this hemispherical shape is distinctly different from the shape of the cubic sample with the matching number of polymer beads and the same cross-link density spread over the interface (shown in Figure 4f). The evolution of spreading of a spherical gel placed close to the oil-water interface is shown in Figure S7. The initial time corresponds to the time instant the gel contacts the interface. Both R_g and κ^2 increase with gel adsorption onto the interface. Despite relatively closely matching values of $\langle R_g \rangle$ for the gels at the interface in equilibrium, with $\langle R_{\rm g} \rangle$ values only slightly smaller for spherical (Figure S7) than for cubic gels, the corresponding shape anisotropies differ significantly. The $\langle \kappa^2 \rangle$, in equilibrium, is approximately two times smaller for a cubic gel (Figure 7d), indicating that the initial symmetry is preserved to a significantly larger extent. Next, we compare the equilibrium extent of spreading of these gels at the interface, α (Figure 7e), and the effective change in thickness in equilibrium (Figure 7f), defined as a ratio of the square root of the smallest

eigenvector of the gyration tensor at the interface, $\sqrt{\lambda_3}$, to the same value in water in equilibrium $\langle \sqrt{\lambda_3^{\text{w}}} \rangle$. (Notably, all three eigenvalues in water are approximately the same.) Figure 7 shows that the most loosely cross-linked gels considered herein stretch approximately by factors of 2.42 and 2.28 for cubic and spherical gels, respectively, while the densely cross-linked gels show significantly lower extent of spreading by a factor of about 1.2 (approximately the same for both shapes). We note that the contact radius normalized by the hydrodynamic radius (a measure similar to the extent of spreading defined above) was shown to decrease with an increase in the cross-linker fraction in the experimental studies of microgels adsorbing and spreading at the liquid-air interface.²¹ Notably, the height of the gel adsorbed at the interface decreases with the decrease in the cross-link density. In all cases considered, the fraction of the gel extending into the water phase is significantly larger for the cubic than for the spherical gels with a matching number of polymer beads and the same cross-link density (Figure 7f). To summarize, we find that the cubic samples of approximately the same initial sizes retain their shapes better than the spherical samples, with the larger fraction of gels extending out into the water phase and a larger range of complex shapes observed for these samples (Figure 4). Hence, the choice of the cubic shape over the spherical one could result in a wider range of topographies that can be dynamically prescribed onto

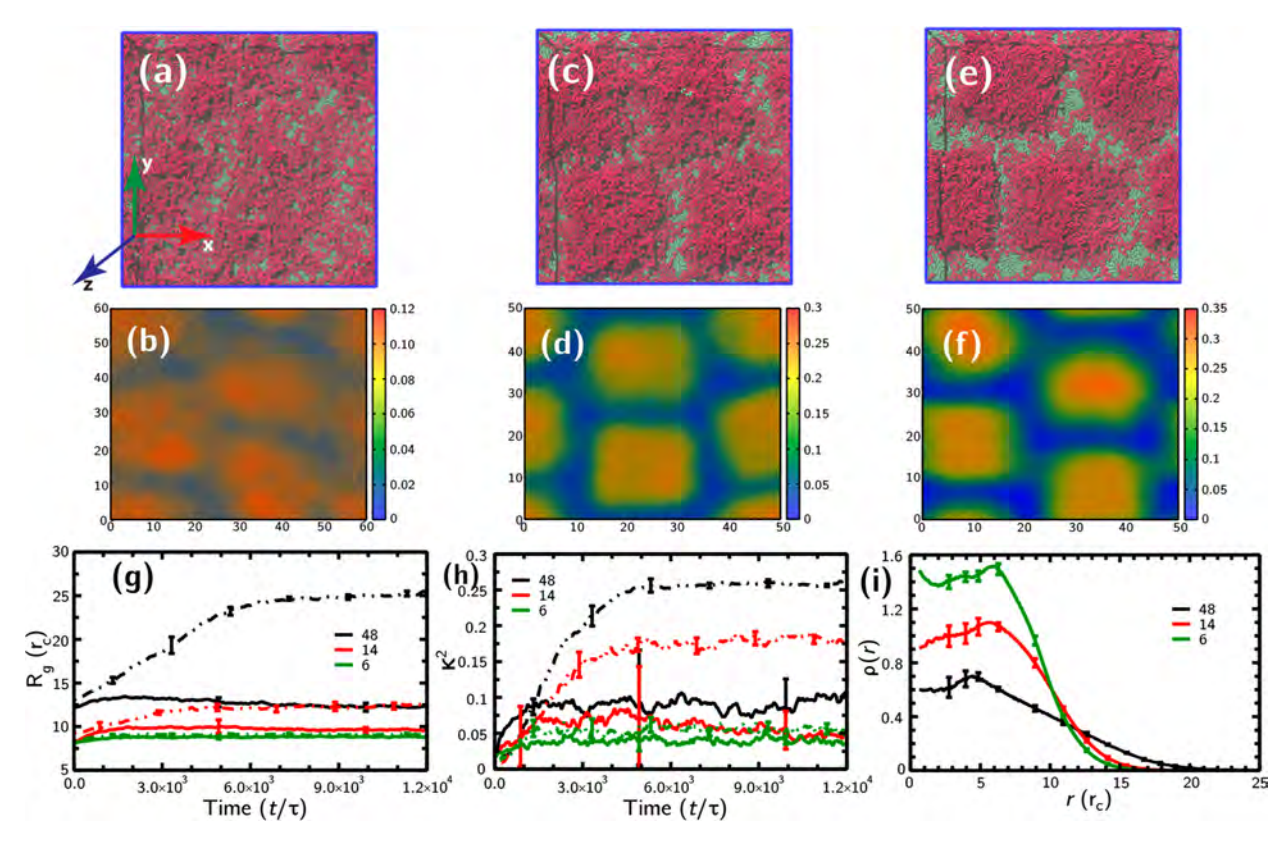


Figure 8. (a–f) Equilibrium gel morphologies and polymer densities for $2 \times 2 \times 2$, $N_x = 48$ (a, b); $3 \times 3 \times 3$, $N_x = 14$ (c, d); and $4 \times 4 \times 4$, $N_x = 6$ (e, f) (the cross-link density increases from left to right). (g) Time evolution of a radius of gyration, R_g , and (h) shape anisotropy, κ^2 , averaged over four gels. Dashed and solid lines, respectively, represent single and multiple gels. (i) Number density of the polymer in equilibrium as a function of its distance from the center, averaged over four gels.

the soft interface when the gels are adsorbed from a solvent onto the soft interfaces.

Multiple Gels at Interfaces as Soft Nanostructured Surfaces. So far, we have focused on a single nanogel adsorption onto the interface. However, for various practical applications the collective behavior of multiple nanogels at the interface is of interest. At relatively high saturation of the gels at interfaces, each gel would interact not only with the solvent but also with neighboring gels. 25,86 Herein, we consider PAAm hydrogels with various cross-link densities (and matching numbers of PAAm beads) at the interface and characterize their time evolution and equilibrium conformations. Four gels with $2 \times 2 \times 2$, $N_x = 48$; $3 \times 3 \times 3$, $N_x = 14$; and $4 \times 4 \times 4$, $N_x = 14$ = 6 are pre-equilibrated in water and then placed in the water phase in close proximity to one of the interfaces. The vertical dimension was chosen to be sufficiently large, and the gel concentration in water is sufficiently low that the gels migrate to and adsorb onto a single interface. Note that the spreading of multiple gels is constrained in the xy plane by the periodic boundary conditions. For the case of multiple gels, the spreading of an individual gel over the interface is controlled not only by the cross-link densities and the size of the samples as discussed above but also by the interactions with the neighboring gels (or interface saturation). Figure 8a-f shows equilibrium gel morphologies (top row) and polymer densities (bottom row) for all three cases (the cross-link density increases from left to right). The evolution of R_g for loosely cross-linked gels ($N_x = 48$) shows a small change from its swollen conformation (Figure 8, black solid line), indicating that the spreading of these gels is strongly restricted with

respect to that of a single gel (case shown in Figure 4; the R_g for a single gel in this case is shown by the black dashed curve). Correspondingly, while a loosely cross-linked single gel flattens at the interface (black dashed line corresponding to $\kappa^2 \approx 0.25$), the same gel as part of an array is only able to reach $\kappa^2 \approx 0.1$ (black solid line) (Figure 8h). On the contrary, the neighboring gels essentially do not interact in the case of most densely cross-linked gels ($N_r = 6$, Figure 8f) so that the dashed (singe gels) and the solid (multiple gels) curves overlap in Figure 8g,h. An intermediate response is observed for gels with $N_x = 14$; the spreading is restricted with respect to the single gel but is not as pronounced as for N_x = 48. In effect, the equilibrium radius of gyration and shape anisotropy saturate to approximately the same values at $N_x = 14$ and 6, indicating a strong dependence on the surface coverage. Finally, the gel density profiles indicate that with an increase in the cross-link density the flattened core-shell morphology with more dense cores extending into the water phase and loosely cross-linked more flattened coronas are observed (Figure 8b,d,f). To quantify this flattened core-shell morphology, we computed the density of the gel beads as a function of their distance from the gel center (r = 0 in Figure 8 is taken at the center of each gel, and curves are averaged over four gels). We calculated the center of mass of each gel and counted the number of gel beads in the $r + \delta r$ volume element for every frame in equilibrium for the last 1200 frames. Then we normalized this value with the volume element and averaged over all of the frames considered. Figure 8 shows that with the decrease in the cross-link density the core is more diffuse (black curve). The densely cross-linked gels maintain a well-defined core and a

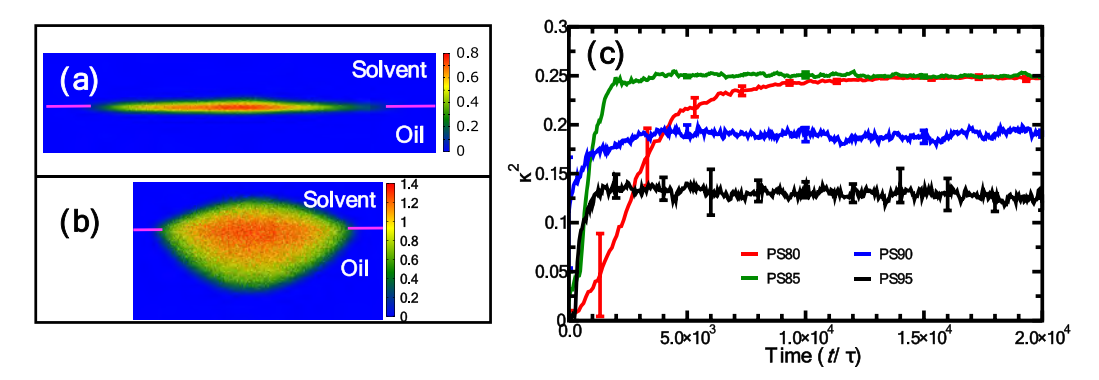


Figure 9. (a, b) Number density profiles (side view) for gels with polymer–solvent repulsion parameter $a_{PS} = 85$ in (a) and $a_{PS} = 95$ in (b) for the densely cross-linked $3 \times 3 \times 3$, $N_x = 30$ gels. (c) Time evolution of the shape anisotropy, κ^2 , for the values of a_{PS} given in the legend.

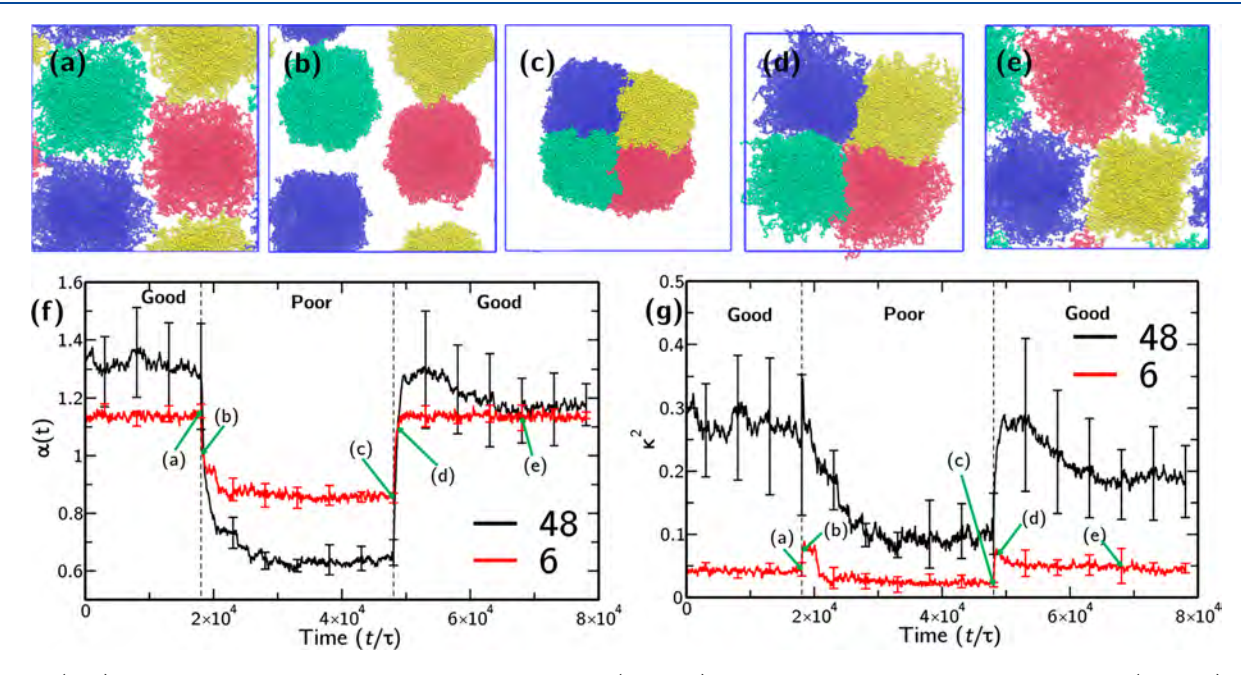


Figure 10. (a–e) Shape changes and aggregation of gels at the interface (top view) upon changing the solvent quality from good ($a_{PS} = 80$) to poor ($a_{PS} = 95$) for $4 \times 4 \times 4$, $N_x = 6$ and then back to the good solvent for the densely cross-linked $4 \times 4 \times 4$, $N_x = 6$ gels. (a) Good solvent. (b) Onset of the poor solvent which equilibrates to (c). (d) Onset of good solvent and equilibration to (e). For clarity of representation, neither solvent nor oil beads are shown. The morphology snapshots correspond to time instances $t = 1.804 \times 10^4$, 1.824×10^4 , 4.804×10^4 , 4.88×10^4 , and $6.804 \times 10^4\tau$ (from left to right). (f, g) Time evolution of the extent of spreading, $\alpha(t)$, in (f) and the shape anisotropy in (g) with the change in solvent quality from good to poor to good. The data are averaged over four gels. Marks (a)–(e) correspond to the snapshots in the upper row. The morphology snapshots for the loosely cross-linked gels are given in Figure S8.

core—shell boundary (green curve in Figure 8i), and this boundary becomes more diffuse with the decrease in cross-link density.

Solvent Quality Effect. In the next series of simulations, we probe the effect of solvent quality by changing the polymer—solvent interaction parameter, $a_{\rm PS}$. First, we focus on the response of a single nanogel (3 × 3 × 3, N_x = 30) to the variations in solvent quality and then on the effects of solvent quality on the interactions between the multiple gels at the interfaces. We varied the polymer—solvent interaction parameter, $a_{\rm PS}$ = (80,85,90,95), mimicking a transition from the good to poor solvent. The change in solvent quality can be achieved via variations in temperature or pH or by illuminating the systems as described above provided that either PAAm copolymerized with various stimuli-responsive moieties or thermoresponsive PNIPAAm-based gels or their copolymers are used. In these series of simulations, we kept the solvent—oil

and polymer-oil interaction parameters the same as above $(a_{SO} = 100 \text{ and } a_{PO} = 85)$ and varied only the polymer-solvent interaction parameter. We find that while for $a_{PS} = 80$ and 85 the gels nearly flatten at the interface, achieving a shape anisotropy of $\kappa^2 \approx 0.25$ (Figure 9a,c), whereas a decrease in the effective quality of solvent with respect to the oil (an increase in a_{PS}) results in a significantly lower extent of spreading and samples protruding into the lower phase deeper than extending into the upper phase (Figure 9b). In other words, it is most energetically favorable for the gel to spread over the interface in the case depicted in Figure 9 since the energy gain due to the shielding of the oil-solvent contacts is high enough to overcome an energy penalty for the chain stretching during the gel restructuring. Notably, in this case the gel protrudes into both phases to the same extent as could be anticipated (an affinity between polymer beads and both upper and lower phases are the same), as was observed in prior studies for the spherical samples.^{20,28} On the contrary, when the quality of the upper solvent drops, the spreading of the same gel into a thin layer is no longer energetically favorable because of the added cost of the gel—solvent interface (Figure 9b); hence, the shape anisotropy remains lower and an extent of spreading significantly decreases (Figure 9c).

To probe the interactions between the multiple nanogels placed within the solvents of various qualities, we decreased the affinity between the polymer and solvent by changing a_{PS} = 80 (good solvent, the same cases as considered in Figure 8a,e) to $a_{PS} = 95$ (poor solvent, the highest polymer-solvent interaction considered in Figure 9), while keeping the remaining system parameters fixed as given above. We analyzed densely and loosely cross-linked nanogels for the system with four gels in a periodic box. Here, we use different colors for each gel to be able to visually distinguish individual gels (Figure 10a-e). It can be seen that individual gels do not interpenetrate and remain clearly distinguishable. The absence of gels' interpenetration has been previously noted in simulations on amphiphilic arborescent microgels⁸⁷ and experiments involving the compression of the interfacial microgel monolayer. 88 We find that upon a drop in solvent quality the individual gels first shrink (Figure 10b) and then agglomerate into a single cluster (Figure 10c). We note that this behavior is consistent with gel aggregation upon the decrease in solvent quality observed experimentally for spherical gels.⁸⁹ Upon changing the solvent quality back to the good solvent, the gels move away from each other for both densely (Figure 10d,e) and loosely cross-linked gels (Figure S8). The densely cross-linked gels completely recover their initial characteristics relatively quickly (red curves in Figure 10f,g for the extent of spreading and shape anisotropy, respectively). We note, however, that the gel positions are reshuffled with respect to each other after the recovery (compare the same gels in Figure 10a,e). The same characteristics for the loosely cross-linked gels (black curves in Figures 10e,f) are also recovered to a large degree; however, the large error bars corresponding to the averaging over four gels indicate that for the case of loosely cross-linked gels variations between the shapes of individual gels are greater than that for densely cross-linked gels. Overall, the shape anisotropy is lower for densely cross-linked gels in both solvents, indicating that they retain a higher symmetry in any solvent (Figure 10g).

Interestingly, the extent of spreading, α , is higher for the loosely cross-linked gels than for the densely cross-linked samples in a good solvent; however, the tendencies are "flipped" in a poor solvent (Figure 10c). The latter effect could be understood by recalling that each gel not only deswells in poor solvent but is also able to be immersed more deeply in the lower phase (Figure 9b). Therefore, the differences between the extent of spreading in good and poor solvents are expected to be significantly higher for loosely cross-linked than for densely cross-linked gels. The morphologies of the loosely cross-linked gels are shown at the interfaces with changing solvent quality. It is worth noting that while the cluster of four densely cross-linked gels attains approximately a square cross section at the interface (Figure 10c), the cluster of four loosely cross-linked gels has a close to circular cross section (Figure S8b). Finally, the values of the largest linear dimension, $\sqrt{\lambda_1}$, of loosely and densely cross-linked gels within

these distinct four-gel clusters in poor solvent are comparable (Figure S8d).

CONCLUSIONS

We investigated dynamic shape changes and the restructuring of cubic hydrogels upon their adsorption onto the liquidliquid interfaces. We first validated our model parameters with respect to the known experimental values for PAAm gels and focused on spreading and shape changes of PAAm nanogels onto the oil-water interfaces. We then probed the behavior of active hydrogels by changing the affinity of the polymer matrix to the solvent, which can be caused by the application of an external stimulus (light, temperature, and change in the chemical composition of solvent). We had shown that the dynamics of the adsorption and spreading process and an equilibrium shape of the gel is determined by the size, crosslink density, and quality of the solvents. Nanogels reduce interfacial tension by spreading over and to some degree flattening at the interface. We showed that these gels are able to adopt various shapes depending on their physical properties. Loosely cross-linked gels and small gels (low total count of polymer beads) spread significantly and adopt close-to-planar shapes. Densely cross-linked gels and gels of larger sizes adopt various complex shapes owing to a larger contribution from the elasticity of a polymer network that in turn results in the retention of a significant fraction of the gel in the water phase. We quantified an enhancement in the extent of spreading and a deviation from the symmetric equilibrium shapes captured by the shape anisotropy that could be achieved by using loosely cross-linked gels. Furthermore, by comparing the spreading of gels of spherical and cubical shapes, we showed that the cubic samples of approximately the same initial sizes were able to retain their shapes significantly better, with the larger fraction of gels extending out into the water phase. Our results show that the choice of the cubic shape over the spherical one results in a wider range of topographies that can be dynamically prescribed onto the soft interface upon the gels' adsorption.

We then probed the structural transitions in gels and nanostructured interfaces containing multiple gels and focused on the response of these nanostructured surfaces to solvent quality caused by a variation in external stimuli. We showed that when the solvent quality changes from good to poor the nanogels that are adsorbed at the interface first shrink and then aggregate into a cluster that has either an approximately square cross section in the interface plane for the densely cross-linked gels or an approximately circular cross section for the loosely cross-linked gels. Upon changing the solvent quality back to the good solvent, the gels move away from each other. These results show that controlling the shapes and clustering of the gels at the interfaces by means of changing solvent quality results in tailoring the dynamics and topography of soft nanostructured interfaces. Hence our findings provide insights into the design of soft active nanostructured surfaces with topographies controlled externally via solvent quality.

ASSOCIATED CONTENT

Supporting Information

The Supporting Information is available free of charge at https://pubs.acs.org/doi/10.1021/acs.langmuir.9b03486.

Details of hydrogels geometries; repulsion parameters used in simulations; box dimensions, number of polymer, oil, and solvent beads; snapshots for the $2 \times$

 2×2 , $3 \times 3 \times 3$, and $4 \times 4 \times 4$ $N_x = 30$ gels at the interface; plot of R_g vs N_x ; time evolution of R_g/N_x as a function of time; effect of mSRP on gel adsorption of $4 \times 4 \times 4$ $N_x = 6$ gel; κ^2 for four simulations with varying initial velocities; time evolution of R_g and κ^2 for spherical gel; shape changes and aggregation in gels at interfaces with changing solvent quality $(2 \times 2 \times 2 N_x = 48)$ (PDF)

AUTHOR INFORMATION

Corresponding Author

Olga Kuksenok — Department of Materials Science and Engineering, Clemson University, Clemson, South Carolina 29634, United States; orcid.org/0000-0002-1895-5206; Phone: 1-864-656-5956; Email: okuksen@clemson.edu

Authors

Chandan Kumar Choudhury — Department of Materials Science and Engineering, Clemson University, Clemson, South Carolina 29634, United States; orcid.org/0000-0002-8449-5690

Vaibhav Palkar — Department of Materials Science and Engineering, Clemson University, Clemson, South Carolina 29634, United States

Complete contact information is available at: https://pubs.acs.org/10.1021/acs.langmuir.9b03486

Notes

The authors declare no competing financial interest.

ACKNOWLEDGMENTS

O.K. gratefully acknowledges partial support of the National Science Foundation EPSCoR Program (award no. OIA-1655740), partial support of the American Chemical Society Petroleum Research Fund (grant no. 56632-ND7), and partial support of the National Science Foundation MRI (award no. 1725573). Clemson University is acknowledged for computational time on the Palmetto cluster.

REFERENCES

- (1) Oliver, K.; Seddon, A.; Trask, R. S. Morphing in nature and beyond: a review of natural and synthetic shape-changing materials and mechanisms. *J. Mater. Sci.* **2016**, *51* (24), 10663–10689.
- (2) Anselme, K. Osteoblast adhesion on biomaterials. *Biomaterials* **2000**, 21 (7), 667–681.
- (3) Karg, M.; Pich, A.; Hellweg, T.; Hoare, T.; Lyon, L. A.; Crassous, J. J.; Suzuki, D.; Gumerov, R. A.; Schneider, S.; Potemkin, I. I.; Richtering, W. Nanogels and Microgels: From Model Colloids to Applications, Recent Developments, and Future Trends. *Langmuir* **2019**, *35* (19), 6231–6255.
- (4) Plamper, F. A.; Richtering, W. Functional Microgels and Microgel Systems. Acc. Chem. Res. 2017, 50 (2), 131–140.
- (5) Brugger, B.; Vermant, J.; Richtering, W. Interfacial layers of stimuli-responsive poly-(N-isopropylacrylamide-co-methacrylicacid) (PNIPAM-co-MAA) microgels characterized by interfacial rheology and compression isotherms. *Phys. Chem. Chem. Phys.* **2010**, 12 (43), 14573–14578.
- (6) Ngai, T.; Behrens, S. H.; Auweter, H. Novel emulsions stabilized by pH and temperature sensitive microgels. *Chem. Commun.* **2005**, No. 3, 331–333
- (7) Kim, Y.; Yuk, H.; Zhao, R.; Chester, S. A.; Zhao, X. Printing ferromagnetic domains for untethered fast-transforming soft materials. *Nature* **2018**, 558 (7709), 274–279.

- (8) Savchak, O.; Morrison, T.; Kornev, K. G.; Kuksenok, O. Controlling deformations of gel-based composites by electromagnetic signals within the GHz frequency range. *Soft Matter* **2018**, *14* (43), 8698–8708
- (9) Gong, J. P.; Katsuyama, Y.; Kurokawa, T.; Osada, Y. Double-Network Hydrogels with Extremely High Mechanical Strength. *Adv. Mater.* **2003**, *15* (14), 1155–1158.
- (10) Oh, J. K.; Drumright, R.; Siegwart, D. J.; Matyjaszewski, K. The development of microgels/nanogels for drug delivery applications. *Prog. Polym. Sci.* **2008**, 33 (4), 448–477.
- (11) Gao, D.; Xu, H.; Philbert, M. A.; Kopelman, R. Ultrafine Hydrogel Nanoparticles: Synthetic Approach and Therapeutic Application in Living Cells. *Angew. Chem., Int. Ed.* **2007**, 46 (13), 2224–2227.
- (12) Yu, B.; Cong, H.; Peng, Q.; Gu, C.; Tang, Q.; Xu, X.; Tian, C.; Zhai, F. Current status and future developments in preparation and application of nonspherical polymer particles. *Adv. Colloid Interface Sci.* **2018**, 256, 126–151.
- (13) Xue, B.; Kozlovskaya, V.; Kharlampieva, E. Shaped stimuli-responsive hydrogel particles: syntheses, properties and biological responses. *J. Mater. Chem. B* **2017**, *5* (1), 9–35.
- (14) Shen, Z.; Ye, H.; Yi, X.; Li, Y. Membrane Wrapping Efficiency of Elastic Nanoparticles during Endocytosis: Size and Shape Matter. *ACS Nano* **2019**, *13*, 215.
- (15) Li, J.; Mooney, D. J. Designing hydrogels for controlled drug delivery. *Nature Reviews Materials* **2016**, *1*, 16071.
- (16) Alexander, J. F.; Kozlovskaya, V.; Chen, J.; Kuncewicz, T.; Kharlampieva, E.; Godin, B. Cubical Shape Enhances the Interaction of Layer-by-Layer Polymeric Particles with Breast Cancer Cells. *Adv. Healthcare Mater.* **2015**, 4 (17), 2657–2666.
- (17) Kozlovskaya, V.; Chen, J.; Tedjo, C.; Liang, X.; Campos-Gomez, J.; Oh, J.; Saeed, M.; Lungu, C. T.; Kharlampieva, E. pHresponsive hydrogel cubes for release of doxorubicin in cancer cells. *J. Mater. Chem. B* **2014**, 2 (17), 2494–2507.
- (18) Harrer, J.; Rey, M.; Ciarella, S.; Löwen, H.; Janssen, L. M. C.; Vogel, N. Stimuli-Responsive Behavior of PNiPAm Microgels under Interfacial Confinement. *Langmuir* **2019**, *35* (32), 10512–10521.
- (19) Minato, H.; Murai, M.; Watanabe, T.; Matsui, S.; Takizawa, M.; Kureha, T.; Suzuki, D. The deformation of hydrogel microspheres at the air/water interface. *Chem. Commun.* **2018**, *54* (8), 932–935.
- (20) Gumerov, R. A.; Rumyantsev, A. M.; Rudov, A. A.; Pich, A.; Richtering, W.; Möller, M.; Potemkin, I. I. Mixing of Two Immiscible Liquids within the Polymer Microgel Adsorbed at Their Interface. *ACS Macro Lett.* **2016**, *5* (5), 612–616.
- (21) Mourran, A.; Wu, Y.; Gumerov, R. A.; Rudov, A. A.; Potemkin, I. I.; Pich, A.; Möller, M. When Colloidal Particles Become Polymer Coils. *Langmuir* **2016**, 32 (3), 723–730.
- (22) Choudhury, C. K.; Kuksenok, O. Modeling dynamics of Polyacrylamide Gel in Oil-Water Mixtures: Dissipative Particle Dynamics Approach. MRS Advances 2018, 3 (26), 1469–1474.
- (23) Dong, L.; Agarwal, A. K.; Beebe, D. J.; Jiang, H. Adaptive liquid microlenses activated by stimuli-responsive hydrogels. *Nature* **2006**, 442, 551.
- (24) Wiese, S.; Spiess Antje, C.; Richtering, W. Microgel-Stabilized Smart Emulsions for Biocatalysis. *Angew. Chem., Int. Ed.* **2013**, *52* (2), 576–579.
- (25) Destribats, M.; Lapeyre, V.; Wolfs, M.; Sellier, E.; Leal-Calderon, F.; Ravaine, V.; Schmitt, V. Soft microgels as Pickering emulsion stabilisers: role of particle deformability. *Soft Matter* **2011**, 7 (17), 7689–7698.
- (26) Yan, M.; Ge, J.; Liu, Z.; Ouyang, P. Encapsulation of Single Enzyme in Nanogel with Enhanced Biocatalytic Activity and Stability. *J. Am. Chem. Soc.* **2006**, *128* (34), 11008–11009.
- (27) Beloqui, A.; Kobitski, A. Y.; Nienhaus, G. U.; Delaittre, G. A simple route to highly active single-enzyme nanogels. *Chemical Science* **2018**, 9 (4), 1006–1013.
- (28) Rumyantsev, A. M.; Gumerov, R. A.; Potemkin, I. I. A polymer microgel at a liquid—liquid interface: theory vs. computer simulations. *Soft Matter* **2016**, *12* (32), 6799–6811.

- (29) Geisel, K.; Isa, L.; Richtering, W. Unraveling the 3D Localization and Deformation of Responsive Microgels at Oil/Water Interfaces: A Step Forward in Understanding Soft Emulsion Stabilizers. *Langmuir* **2012**, 28 (45), 15770–15776.
- (30) Liu, Z.; Guo, R.; Xu, G.; Huang, Z.; Yan, L.-T. Entropy-Mediated Mechanical Response of the Interfacial Nanoparticle Patterning. *Nano Lett.* **2014**, *14* (12), 6910–6916.
- (31) Yong, X. Modeling the Assembly of Polymer-Grafted Nanoparticles at Oil-Water Interfaces. *Langmuir* **2015**, 31 (42), 11458–11469.
- (32) Zakrevskyy, Y.; Richter, M.; Zakrevska, S.; Lomadze, N.; von Klitzing, R.; Santer, S. Light-Controlled Reversible Manipulation of Microgel Particle Size Using Azobenzene-Containing Surfactant. *Adv. Funct. Mater.* **2012**, *22* (23), 5000–5009.
- (33) Wei, J.; Yu, Y. Photodeformable polymer gels and crosslinked liquid-crystalline polymers. *Soft Matter* **2012**, *8* (31), 8050–8059.
- (34) Irie, M.; Kunwatchakun, D. Photoresponsive polymers. 8. Reversible photostimulated dilation of polyacrylamide gels having triphenylmethane leuco derivatives. *Macromolecules* **1986**, *19* (10), 2476–2480.
- (35) Ziółkowski, B.; Florea, L.; Theobald, J.; Benito-Lopez, F.; Diamond, D. Self-protonating spiropyran-co-NIPAM-co-acrylic acid hydrogel photoactuators. *Soft Matter* **2013**, *9* (36), 8754–8760.
- (36) Mergel, O.; Schneider, S.; Tiwari, R.; Kühn, P. T.; Keskin, D.; Stuart, M. C. A.; Schöttner, S.; de Kanter, M.; Noyong, M.; Caumanns, T.; Mayer, J.; Janzen, C.; Simon, U.; Gallei, M.; Wöll, D.; van Rijn, P.; Plamper, F. A. Cargo shuttling by electrochemical switching of core—shell microgels obtained by a facile one-shot polymerization. *Chemical Science* **2019**, *10* (6), 1844–1856.
- (37) Plamper, F. A. Changing Polymer Solvation by Electrochemical Means: Basics and Applications. In *Porous Carbons Hyperbranched Polymers Polymer Solvation*; Long, T. E., Voit, B., Okay, O., Eds.; Springer International Publishing: Cham, 2015; pp 125–212.
- (38) Mergel, O.; Wünnemann, P.; Simon, U.; Böker, A.; Plamper, F. A. Microgel Size Modulation by Electrochemical Switching. *Chem. Mater.* **2015**, 27 (21), 7306–7312.
- (39) Wu, Y.; Wiese, S.; Balaceanu, A.; Richtering, W.; Pich, A. Behavior of Temperature-Responsive Copolymer Microgels at the Oil/Water Interface. *Langmuir* **2014**, 30 (26), 7660–7669.
- (40) Gumerov, R. A.; Gau, E.; Xu, W.; Melle, A.; Filippov, S. A.; Sorokina, A. S.; Wolter, N. A.; Pich, A.; Potemkin, I. I. Amphiphilic PVCL/TBCHA microgels: from synthesis to characterization in a highly selective solvent. *J. Colloid Interface Sci.* **2020**, *564*, 344.
- (41) Ramos, J.; Imaz, A.; Forcada, J. Temperature-sensitive nanogels: poly(N-vinylcaprolactam) versus poly(N-isopropylacrylamide). *Polym. Chem.* **2012**, 3 (4), 852–856.
- (42) Richtering, W. Responsive Emulsions Stabilized by Stimuli-Sensitive Microgels: Emulsions with Special Non-Pickering Properties. *Langmuir* **2012**, 28 (50), 17218–17229.
- (43) Qi, H.; Ghodousi, M.; Du, Y.; Grun, C.; Bae, H.; Yin, P.; Khademhosseini, A. DNA-directed self-assembly of shape-controlled hydrogels. *Nat. Commun.* **2013**, *4* (1), 2275.
- (44) Geng, J.; Pu, J.; Wang, L.; Bai, B. Surface charge effect of nanogel on emulsification of oil in water for fossil energy recovery. *Fuel* **2018**, 223, 140–148.
- (45) Chan, M.; Almutairi, A. Nanogels as imaging agents for modalities spanning the electromagnetic spectrum. *Mater. Horiz.* **2016**, 3 (1), 21–40.
- (46) Lu, S.; Neoh, K. G.; Huang, C.; Shi, Z.; Kang, E.-T. Polyacrylamide hybrid nanogels for targeted cancer chemotherapy via co-delivery of gold nanoparticles and MTX. *J. Colloid Interface Sci.* **2013**, *412*, 46–55.
- (47) Lu, S.; Neoh, K. G.; Kang, E.-T.; Mahendran, R.; Chiong, E. Mucoadhesive polyacrylamide nanogel as a potential hydrophobic drug carrier for intravesical bladder cancer therapy. *Eur. J. Pharm. Sci.* **2015**, 72, 57–68.
- (48) Groot, R. D.; Rabone, K. L. Mesoscopic Simulation of Cell Membrane Damage, Morphology Change and Rupture by Nonionic Surfactants. *Biophys. J.* **2001**, *81* (2), 725–736.

- (49) Groot, R. D.; Warren, P. B. Dissipative particle dynamics: Bridging the gap between atomistic and mesoscopic simulation. *J. Chem. Phys.* **1997**, 107 (11), 4423–4435.
- (50) Groot, R. D. A Local Galilean Invariant Thermostat. J. Chem. Theory Comput. 2006, 2 (3), 568-574.
- (51) Nikunen, P.; Karttunen, M.; Vattulainen, I. How would you integrate the equations of motion in dissipative particle dynamics simulations? *Comput. Phys. Commun.* **2003**, *153* (3), 407–423.
- (52) Español, P.; Warren, P. B. Perspective: Dissipative particle dynamics. J. Chem. Phys. 2017, 146 (15), 150901.
- (53) Warren, P. E. a. P. Statistical Mechanics of Dissipative Particle Dynamics. *EPL (Europhysics Letters)* **1995**, 30 (4), 191.
- (54) Plimpton, S. Fast Parallel Algorithms for Short-Range Molecular Dynamics. *J. Comput. Phys.* **1995**, *117* (1), 1–19.
- (55) LAMMPS Molecular Dynamics Simulator; http://lammps.sandia.gov.
- (56) Širk, T. W.; Slizoberg, Y. R.; Brennan, J. K.; Lisal, M.; Andzelm, J. W. An enhanced entangled polymer model for dissipative particle dynamics. *J. Chem. Phys.* **2012**, *136* (13), 134903.
- (57) Nossal, R. Network formation in polyacrylamide gels. *Macromolecules* **1985**, *18* (1), 49–54.
- (58) Comic, L.; Nagy, B. A topological coordinate system for the diamond cubic grid. *Acta Crystallogr., Sect. A: Found. Adv.* **2016**, 72 (5), 570–581.
- (59) Yong, X.; Kuksenok, O.; Matyjaszewski, K.; Balazs, A. C. Harnessing Interfacially-Active Nanorods to Regenerate Severed Polymer Gels. *Nano Lett.* **2013**, *13* (12), 6269–6274.
- (60) Jha, P. K.; Zwanikken, J. W.; Detcheverry, F. A.; de Pablo, J. J.; Olvera de la Cruz, M. Study of volume phase transitions in polymeric nanogels by theoretically informed coarse-grained simulations. *Soft Matter* **2011**, *7* (13), 5965–5975.
- (61) Vishnyakov, A.; Mao, R.; Lee, M.-T.; Neimark, A. V. Coarse-grained model of nanoscale segregation, water diffusion, and proton transport in Nafion membranes. *J. Chem. Phys.* **2018**, *148* (2), No. 024108.
- (62) Nair, N.; Park, M.; Handgraaf, J.-W.; Cassiola, F. M. Coarse-Grained Simulations of Polymer-Grafted Nanoparticles: Structural Stability and Interfacial Behavior. *J. Phys. Chem. B* **2016**, *120* (35), 9523–9539.
- (63) Duan, M.; Song, X.; Zhao, S.; Fang, S.; Wang, F.; Zhong, C.; Luo, Z. Layer-by-Layer Assembled Film of Asphaltenes/Polyacrylamide and Its Stability of Water-in-Oil Emulsions: A Combined Experimental and Simulation Study. *J. Phys. Chem. C* **2017**, *121* (8), 4332–4342.
- (64) Suekama, T. C.; Aziz, V.; Mohammadi, Z.; Berkland, C.; Gehrke, S. H. Synthesis and characterization of poly(N-vinyl formamide) hydrogels-A potential alternative to polyacrylamide hydrogels. J. Polym. Sci., Part A: Polym. Chem. 2013, 51 (2), 435–445.
- (65) Kizilay, M. Y.; Okay, O. Effect of Initial Monomer Concentration on Spatial Inhomogeneity in Poly(acrylamide) Gels. *Macromolecules* **2003**, *36* (18), 6856–6862.
- (66) Rubinstein, M.; Colby, R. H. Polymer Physics; Oxford University Press: Oxford, U.K., 2003.
- (67) Pivkin, I. V.; Caswell, B.; Karniadakis, G. E. Dissipative Particle Dynamics. In *Reviews in Computational Chemistry*; Lipkowitz, K. B., Ed.; John Wiley & Sons: Hoboken, NJ, 2011; Vol. 27, pp 85–110.
- (68) Gumerov, R. A.; Filippov, S. A.; Richtering, W.; Pich, A.; Potemkin, I. I. Amphiphilic microgels adsorbed at oil-water interfaces as mixers of two immiscible liquids. *Soft Matter* **2019**, *15* (19), 3978–3986.
- (69) Geisel, K.; Rudov, A. A.; Potemkin, I. I.; Richtering, W. Hollow and Core-Shell Microgels at Oil-Water Interfaces: Spreading of Soft Particles Reduces the Compressibility of the Monolayer. *Langmuir* **2015**, *31* (48), 13145–13154.
- (70) Flory, P. J. Principles of Polymer Chemistry; Cornell University Press: 1953.
- (71) Lopez, C. G.; Richtering, W. Does Flory-Rehner theory quantitatively describe the swelling of thermoresponsive microgels? *Soft Matter* **2017**, *13* (44), 8271–8280.

- (72) Kizilay, M. Y.; Okay, O. Effect of swelling on spatial inhomogeneity in poly (acrylamide) gels formed at various monomer concentrations. *Polymer* **2004**, *45* (8), 2567–2576.
- (73) Geissler, E.; Hecht, A. M.; Horkay, F.; Zrinyi, M. Compressional modulus of swollen polyacrylamide networks. *Macromolecules* **1988**, 21 (8), 2594–2599.
- (74) Akagi, Y.; Gong, J. P.; Chung, U.; Sakai, T. Transition between Phantom and Affine Network Model Observed in Polymer Gels with Controlled Network Structure. *Macromolecules* **2013**, *46* (3), 1035–1040.
- (75) Pritchard, R. H.; Terentjev, E. M. Swelling and de-swelling of gels under external elastic deformation. *Polymer* **2013**, *54* (26), 6954–6960.
- (76) Nikolov, S.; Fernandez-Nieves, A.; Alexeev, A. Mesoscale modeling of microgel mechanics and kinetics through the swelling transition. *Applied Mathematics and Mechanics-English Edition* **2018**, 39 (1), 47–62.
- (77) Chen, S.; Yong, X. Dissipative particle dynamics modeling of hydrogel swelling by osmotic ensemble method. *J. Chem. Phys.* **2018**, 149 (9), No. 094904.
- (78) Day, J. C.; Robb, I. D. Thermodynamic parameters of polyacrylamides in water. *Polymer* **1981**, 22 (11), 1530–1533.
- (79) Mark, J. E. *Polymer Data Handbook*, 2nd ed.; Oxford University Press: Oxford, U.K., 2009.
- (80) Chen, S. S.; Yong, X. Dissipative particle dynamics modeling of hydrogel swelling by osmotic ensemble method. *J. Chem. Phys.* **2018**, 149 (9), 094904.
- (81) Sato, K.; Nakajima, T.; Hisamatsu, T.; Nonoyama, T.; Kurokawa, T.; Gong, J. P. Phase-Separation-Induced Anomalous Stiffening, Toughening, and Self-Healing of Polyacrylamide Gels. *Adv. Mater.* **2015**, 27 (43), 6990.
- (82) Theodorou, D. N.; Suter, U. W. Shape of unperturbed linear polymers: polypropylene. *Macromolecules* **1985**, *18* (6), 1206–1214.
- (83) Moreno, N.; Nunes, S. P.; Peinemann, K.-V.; Calo, V. M. Topology and Shape Control for Assemblies of Block Copolymer Blends in Solution. *Macromolecules* **2015**, *48* (21), 8036–8044.
- (84) Bosko, J. T.; Todd, B. D.; Sadus, R. J. Analysis of the shape of dendrimers under shear. J. Chem. Phys. 2006, 124 (4), No. 044910.
- (85) Lee, H.; Baker, J. R.; Larson, R. G. Molecular Dynamics Studies of the Size, Shape, and Internal Structure of 0% and 90% Acetylated Fifth-Generation Polyamidoamine Dendrimers in Water and Methanol. *J. Phys. Chem. B* **2006**, *110* (9), 4014–4019.
- (86) Pinaud, F.; Geisel, K.; Massé, P.; Catargi, B.; Isa, L.; Richtering, W.; Ravaine, V.; Schmitt, V. Adsorption of microgels at an oil—water interface: correlation between packing and 2D elasticity. *Soft Matter* **2014**, *10* (36), 6963–6974.
- (87) Gumerov, R. A.; Rudov, A. A.; Richtering, W.; M?ller, M.; Potemkin, I. I. Amphiphilic Arborescent Copolymers and Microgels: From Unimolecular Micelles in a Selective Solvent to the Stable Monolayers of Variable Density and Nanostructure at a Liquid Interface. ACS Appl. Mater. Interfaces 2017, 9 (37), 31302–31316.
- (88) Scotti, A.; Bochenek, S.; Brugnoni, M.; Fernandez-Rodriguez, M. A.; Schulte, M. F.; Houston, J. E.; Gelissen, A. P. H.; Potemkin, I. I.; Isa, L.; Richtering, W. Exploring the colloid-to-polymer transition for ultra-low crosslinked microgels from three to two dimensions. *Nat. Commun.* **2019**, *10*, 8.
- (89) Brugger, B.; Richtering, W. Emulsions stabilized by stimulisensitive poly(N-isopropylacrylamide)-co-methacrylic acid polymers: Microgels versus low molecular weight polymers. *Langmuir* **2008**, 24 (15), 7769–7777.